AGU PUBLICATIONS

JGR

Journal of Geophysical Research: Atmospheres

RESEARCH ARTICLE
10.1002/2015JD023700

**Key Points:**
- Geometry features of the vortex are shown
- Evolution mechanisms of the vortex are shown
- Interactions of systems of various scales are shown

**Supporting Information:**
- Text S1

**Correspondence to:**
J. Ling,
Lingjian@lasg.iap.ac.cn

**Citation:**
Fu, S.-M., W.-L. Li, and J. Ling (2015), On the evolution of a long-lived mesoscale vortex over the Yangtze River Basin: Geometric features and interactions among systems of different scales, *J. Geophys. Res. Atmos.*, *120*, doi:10.1002/2015JD023700.

Received 20 MAY 2015
Accepted 4 NOV 2015
Accepted article online 7 NOV 2015



# On the evolution of a long-lived mesoscale vortex over the Yangtze River Basin: Geometric features and interactions among systems of different scales

**Shen-Ming Fu[1], Wan-Li Li[2], and Jian Ling[3]**

[1]International Center for Climate and Environment Sciences, Institute of Atmospheric Physics, Chinese Academy of Sciences, Beijing, China, [2]China Meteorological Administration Training Center, Beijing, China, [3]LASG, Institute of Atmospheric Physics, Chinese Academy of Sciences, Beijing, China

**Abstract** A long-lived mesoscale vortex that caused extremely heavy rainfall events over the Yangtze River Basin was reproduced reasonably by the advanced Weather Research and Forecasting model. Using simulations, the three-dimensional geometric features of the vortex, as well as the interactions between the vortex and its background circulations (BCs), were investigated. Results indicated that the geometry features of the vortex were closely related to vortex evolution, vortex-related convection processes and precipitation, and vortex-BC interactions. Growth in the horizontal size of the vortex favored its sustainment. The vortex tended to produce stronger convection processes and precipitation as its orientation became closer to the west-east direction. The circulation budget revealed that the convergence-related shrinking, the BC transport, and the effects caused by vortex movement were the dominant factors for vortex development. Divergence-related stretching dominated vortex dissipation, and the transport effects associated with the BC and the eddy flows also accelerated this attenuation. The energy budget indicated that the vortex intensely interacted with its BCs during its lifetime. The BCs affected the vortex through downscaled energy cascade and mean transport; the eddy flow reacted to its BCs via upscaled energy cascade and eddy transport. Generally, the vortex had more dynamic than thermodynamic interactions with its BCs. BC effects were vital to the vortex evolution, whereas the variation in the BCs was predominantly determined by their own effects, although the reaction of the vortex-related eddy flow cannot be ignored in the variation of the BC dynamical fields.

## 1. Introduction

Heavy rainfall events are one of the most severe natural disasters worldwide [*Tao and Ding*, 1981; *Karl and Knight*, 1998; *Speer*, 2008; *Black*, 2009; *Stevenson and Schumacher*, 2014; *Qian et al.*, 2015]. It is known that mesoscale vortices are important triggers for these torrential rainfall events [*Ninomiya*, 2000; *Kirk*, 2003; *Zhao et al.*, 2004; *Shen et al.*, 2005; *James and Johnson*, 2010; *Fu et al.*, 2013, 2014]. In China, the Yangtze River Basin (Figure 1) experiences the most severe summer rainfall [*Tao*, 1980; *Ding et al.*, 2007]. Frequent mesoscale vortices cause a significant proportion of the total accumulated precipitation over this region [*Zhao et al.*, 2004]. The extreme torrential rainfall events, which persist for several days and cause flash floods, substantial casualties, and huge economic losses, are more closely related to these mesoscale vortices [*Kuo et al.*, 1988; *Hu and Pan*, 1996; *Shen et al.*, 2005; *Zhao and Fu*, 2007; *Sun et al.*, 2010; *Yang et al.*, 2010; *Fu et al.*, 2011].

For decades, mesoscale vortices over the Yangtze River Basin have been a hot research topic because of their significant importance. Statistical studies [*Lu*, 1986; *Chen et al.*, 2007; *Yang et al.*, 2010; *Fu et al.*, 2014] have shown that, over this area, the mesoscale vortices occur very frequently from spring to autumn and that the sources of these vortices are primarily located around the Sichuan Basin and the Dabie Mountain region (Figure 1). These mesoscale vortices are highly capable of triggering precipitation, particularly the long-lived cases [*Tao*, 1980; *Kuo et al.*, 1988; *Chen et al.*, 2007; *Fu et al.*, 2014]. Structural analyses [*Zhao and Fu*, 2007; *Yang et al.*, 2010; *Fu et al.*, 2014] have indicated that these mesoscale vortices generally belong to a type of meso-α weather system [*Orlanski*, 1975] and are mainly located in the lower and middle troposphere, with a radius of approximately 200–500 km. Dynamical diagnostic studies have shown that the background circulations

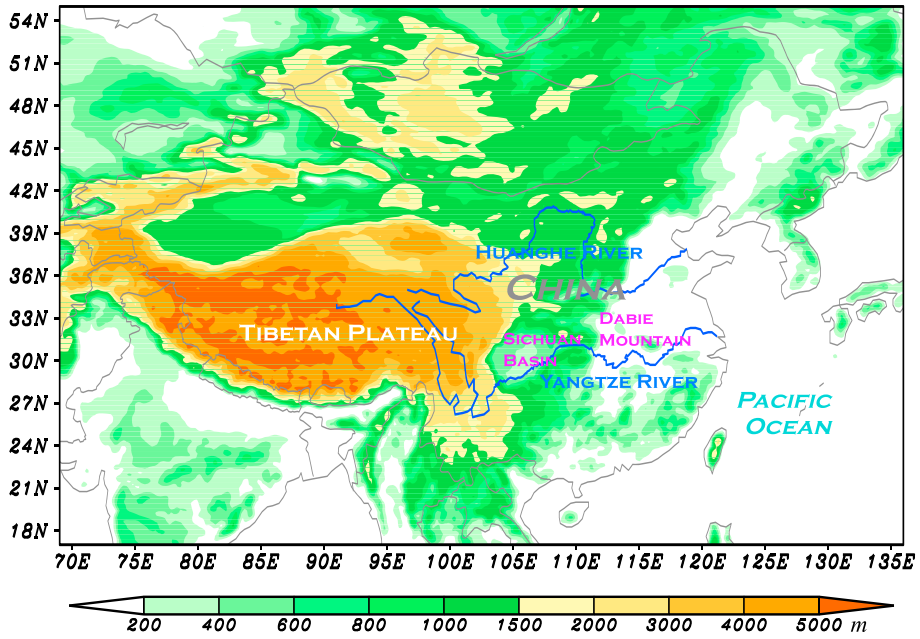


**Figure 1.** Terrain features of the Yangtze River Basin (shaded areas, units: m).

(BCs), including the South Asian High, the 500 hPa shortwave trough, the northwestern Pacific subtropical high, and the Mei-yu front, may significantly affect the evolution of these vortices [*Lu*, 1986; *Zhao and Fu*, 2007; *Sun et al*., 2010; *Fu et al*., 2013]. Energetic studies of these mesoscale vortices [*Fu et al*., 2011, 2014] have proposed that the available potential energy acts as an important energy source for vortex evolution through baroclinic energy conversion. In addition, the terrain features of the Yangtze River Basin are vital for determining the vortex characteristics [*Kuo et al*., 1988; *Wang and Tan*, 2014].

The studies mentioned above have provided detailed information on mesoscale vortices over the Yangtze River Basin. However, it should be noted that, in most of these studies, the horizontal geometry of the mesoscale vortex was determined subjectively. In addition, the vertical extent of the vortex was not discussed in great detail. Thus, the three-dimensional geometry of the mesoscale vortex and its relationship to the main features of the vortex remain unclear. Moreover, although the evolution mechanisms and energy conversion features of the mesoscale vortices have been demonstrated in some previous studies [*Sun et al*., 2010; *Fu et al*., 2013], the interactions between the vortex and its BCs, particularly the reactions of the vortex to its BCs, have rarely been discussed. Therefore, the aims of this study are to present the variation of the mesoscale vortex's three-dimensional geometry against a unified standard, to reveal the relationship between vortex geometry and the vortex's main features, and to quantitatively investigate the interactions between the mesoscale vortex and its BCs.

## 2. Data, Model Configuration, and Methodology

### 2.1. Data and Model Configuration

The advanced Weather Research and Forecasting (WRF) model, version 3.5.1 [*Michalakes et al*., 2004], was used in this study. The 6-hourly, 0.5° × 0.5° Climate Forecast System Reanalysis data, version 2, from the National Centers for Environmental Prediction [*Saha et al*., 2010], was used for the initial and boundary conditions of the simulations. The Chinese Meteorological Administration 3-hourly surface observations and 12-hourly soundings were used to improve the first guess of the outer domain through the objective analysis method. Observational data were also used in the validation of the simulation results. Two domains of one-way nesting were used in the simulations. The horizontal resolutions of the outer and inner domains were 36 km and 12 km, with 301 × 229 and 415 × 265 grid points, respectively. There were 35 eta levels, with

the model top fixed at 50 hPa. The WRF Single-Moment version 5 cloud microphysics parameterization scheme [*Hong et al*., 2004], the Kain–Fritsch cumulus parameterization [*Kain and Fritsch*, 1990], and the Yonsei University planetary boundary layer scheme [*Hong et al*., 2006] were used.

The model was initiated at 00:00 UTC on 06 June 2013, 15 h before the formation of the vortex, and integrated for 96 h to include the entire vortex lifetime.

### 2.2. Methodology

#### 2.2.1. Estimation of the Vortex's Geometric Characteristics

The method reported by *Rudeva and Gulev* [2007] was used to determine the geometric features of the vortex in this study. First, for each time step of the vortex, the original coordinate system was shifted to the polar coordinate system by collocating the polar coordinate origin to the vortex center. Second, following *Akima* [1970], the geopotential height was interpolated onto 36 radii (0° was defined as east, with an angular step of 10°) of the vortex, at a radial spatial step of 1 km. Third, along each of the 36 radii, the $\partial$(geopotential height)/$\partial r$ = 0.1 geopotential meter (gpm) km$^{-1}$ was calculated, within the range of 60–600 km, where $r$ is the radius; thus, a first guess radius and a corresponding critical geopotential height value for that given radius were determined. Fourth, the minimum of all the 36 critical geopotential height values was identified and the locations of the minimum critical geopotential height were interpolated along all other radii. Thus, a closed curve $M$ connecting all 36 critical positions was determined and used to represent the horizontal geometry of the vortex. The area $S_M$ surrounded by the closed curve $M$ was calculated, and the vortex's effective radius was defined as $r_{ef} = \sqrt{S_M/\pi}$. The maximum diameter $d_{\max}$ of the closed curve was determined, and the minimum diameter $d_{\min}$ within ±20° of the diameter orthogonal to the largest diameter was identified. Then, the asymmetry of the vortex was defined as $d_{\max}/d_{\min}$. A vortex was identified if a closed vortex center in the stream field coupled with a significant cyclonic vorticity center ($\geq 10^{-4}$ s$^{-1}$) was detected. The vertical extent of this vortex was determined by checking all the consecutive vertical levels satisfying the above vortex criterion, at a step of 25 hPa [*Fu et al*., 2014].

#### 2.2.2. The Eddy Flux Circulation Budget

In this study, the eddy flux circulation budget, which can evaluate the respective effects of BCs and the eddy flow, was used to examine the evolution mechanisms of the vortex. The eddy flux circulation budget equation was first derived by *Davis and Galarneau* [2009] and rewritten in a quasi-Lagrangian form by *Fu and Sun* [2012] as

$$\underset{\text{ME}}{\frac{\delta C}{\delta t}} = \underset{\text{STR}}{\mathbf{M}_h \cdot \nabla_h C - \overline{\eta}\,\widetilde{\delta} A} - \underset{\text{MT}}{\oint \eta' \overline{\mathbf{V_h}} \cdot \mathbf{n} dl} - \underset{\text{ET}}{\oint \eta' \mathbf{V_h}' \cdot \mathbf{n} dl} + \underset{\text{TIL}}{\oint \omega \left( \mathbf{k} \times \frac{\partial \mathbf{V_h}}{\partial p} \right) \cdot \mathbf{n} dl} + \text{RES}, \tag{1}$$

where the operator $\frac{\delta}{\delta t} = \left( \frac{\partial}{\partial t} + \mathbf{M}_h \cdot \nabla_h \right)$ represents the quasi-Lagrangian variation; $\mathbf{M}_h$ denotes the horizontal moving speed of the target system; subscript $h$ denotes the horizontal component; $\nabla_h = \frac{\partial}{\partial x}\mathbf{i} + \frac{\partial}{\partial y}\mathbf{j}$; $C = \oint \mathbf{V}_h \cdot \mathrm{d}\mathbf{l}$ stands for the circulation along the system boundary; $\mathbf{V}_h = u\mathbf{i} + v\mathbf{j}$ is the horizontal wind field; $\eta$ is the absolute vorticity; $\widetilde{\delta}$ is the system-area-averaged divergence; $A$ is the horizontal area of the target system; $\omega$ is the vertical velocity in the pressure coordinate; **n** is the unit vector normal to the boundary line of the system; **i**, **j**, and **k** are the unit vectors pointing to the east, north, and zenith, respectively; and $p$ is the pressure. The overbar denotes the average around the perimeter of the target system, and the prime represents the perturbation from this mean state.

Term $\mathbf{M}_h \cdot \nabla_h C$ denotes the motion-caused effect (ME) that is due to movement of the target system and the corresponding circulation change; $-\overline{\eta}\,\widetilde{\delta} A$ represents the stretching effects (STR) associated with the target system's divergence; $-\oint \eta' \overline{\mathbf{V_h}} \cdot \mathbf{n} dl$ stands for the mean transport (MT) of the perturbation absolute vorticity; $-\oint \eta' \mathbf{V_h}' \cdot \mathbf{n} dl$ denotes the eddy transport (ET) of the perturbation absolute vorticity; $\oint \omega \left( \mathbf{k} \times \frac{\partial \mathbf{V_h}}{\partial p} \right) \cdot \mathbf{n} dl$ represents the tilting effect (TIL) of both the mean and the eddy flows; and RES represents the effects due to friction, subgrid processes, and calculation uncertainties (Table 1).

**Table 1.** Abbreviations Used in This Study

| Abbreviation | Original Terminology | Abbreviation | Original Terminology |
|---|---|---|---|
| BC | Background circulation | MTKM | Mean transport of $k_m$ |
| $r_{ef}$ | Effective radius | RSW | Reynolds stress work on the mean flow |
| $d_{\max}$ | Maximum diameter | MSM | Molecular stress effect on the mean flow |
| $d_{\min}$ | Minimum diameter | CKMT | Conversion between $k_m$ and $k_t$ |
| ME | Motion-caused effect | BCM | Baroclinic energy conversion (mean flow) |
| STR | Stretching effects | MDM | Molecular dissipation of $k_m$ |
| MT | Mean transport | MTEM | Mean transport of $e_m$ |
| ET | Eddy transport | ETH | Effects of eddy transport of heat |
| TIL | Tilting effect | WMP | Work of the mean pressure |
| TOT | Total term | CEMT | Conversion between $e_m$ and $e_t$ |
| KE | Kinetic energy | GEM | Generation of $e_m$ due to diabatic processes |
| $k_m$ | Mean kinetic energy | TKT | Transport of $k_t$ by the mean and eddy flows |
| $k_t$ | Perturbation kinetic energy | MSE | Molecular stress effect on the eddy flow |
| $e_m$ | Mean exergy | BCE | Baroclinic energy conversion (eddy flow) |
| $e_t$ | Perturbation exergy | MDE | Molecular dissipation of $k_t$ |
| DVS | Developing stage | TET | Transport of $e_t$ by the mean and eddy flows |
| EMS | Early maintaining stage | WPP | Work of the perturbation pressure |
| LMS | Late maintaining stage | GET | Generation of $e_t$ due to diabatic processes |
| DCS | Decaying stage | KPs 1–9 | Kinetic energy separate parts 1–9 |
| Q1–Q4 | Quadrants 1–4 | EPs 1–3 | Exergy separate parts 1–3 |

### 2.2.3. Eddy Kinetic Energy Budget

In this study, the eddy kinetic energy (KE) budget method, reported by *Kucharski and Thorpe* [2000], was employed to investigate the interactions between the vortex and its BCs. A concise form of the equations is

$$\frac{\partial(\overline{\rho}k_m)}{\partial t} = -\nabla\cdot\left[\overline{\rho}\langle\mathbf{V}\rangle k_m + \langle\mathbf{V}\rangle\cdot\overline{\rho\mathbf{V}''\mathbf{V}''} + \overline{\mathbf{F}}\cdot\langle\mathbf{V}\rangle\right] - C\left(\overline{\rho}k_m,\overline{\rho k_t}\right) - C(\overline{\rho}k_m,\overline{\rho}e_m) - D(\overline{\rho}k_m) \tag{2}$$

MTKM RSW MSM CKMT BCM MDM

$$\frac{\partial(\overline{\rho}e_m)}{\partial t} = -\nabla\cdot\left[\overline{\rho}\langle\mathbf{V}\rangle e_m + \langle T\rangle\eta_m\frac{c_p}{\langle\theta\rangle}\cdot\overline{\rho\mathbf{V}''\theta''} + (\overline{p}-p_R)\langle\mathbf{V}\rangle\right] - C(\overline{\rho}e_m,\overline{\rho e_t}) + C(\overline{\rho}k_m,\overline{\rho}e_m) + G(\overline{\rho}e_m) \tag{3}$$

MTEM ETH WMP CEMT BCM GEM

$$\frac{\partial\left(\overline{\rho k_t}\right)}{\partial t} = -\nabla\cdot\left[\overline{\rho\mathbf{V}k_t} + \overline{\mathbf{F}\cdot\mathbf{V}''}\right] + C\left(\overline{\rho}k_m,\overline{\rho k_t}\right) + C\left(\overline{\rho k_t},\overline{\rho e_t}\right) - D\left(\overline{\rho k_t}\right) \tag{4}$$

TKT MSE CKMT BCE MDE

$$\frac{\partial\left(\overline{\rho e_t}\right)}{\partial t} = -\nabla\cdot\left[\overline{\rho\mathbf{V}e_t} + \overline{p'\mathbf{V}''}\right] + C(\overline{\rho}e_m,\overline{\rho e_t}) - C\left(\overline{\rho k_t},\overline{\rho e_t}\right) + G(\overline{\rho e_t}), \tag{5}$$

TET WPP CEMT BCE GET

where the overbar indicates a zonal average. For a variable $\psi$, $\langle\psi\rangle = \frac{\overline{\rho\psi}}{\overline{\rho}}$ represents its density-weighted average, where $\rho$ is the density and the corresponding perturbation is defined as $\psi'' = \psi - \langle\psi\rangle$. The terms $k_m = \frac{1}{2}\langle\mathbf{V}\rangle\cdot\langle\mathbf{V}\rangle$ and $k_t = \frac{1}{2}\mathbf{V}''\cdot\mathbf{V}''$ represent the mean KE and the perturbation KE, respectively; $e_m$ and $e_t$ denote the mean exergy and the perturbation exergy, respectively, where the exergy is a local formulation of the global available potential energy [*Kucharski and Thorpe*, 2000]; $T$ is the temperature; $\eta_m$ is the mean Carnot factor, $c_p$ is the specific heat of dry air at constant pressure; $\theta$ is the potential temperature; the subscript $R$ denotes the reference state; and $\mathbf{F}$ is the molecular stress tensor.

Term $-\nabla\cdot[\overline{\rho}\langle\mathbf{V}\rangle k_m]$ denotes the mean transport of $k_m$ (MTKM), $-\nabla\left[\langle\mathbf{V}\rangle\cdot\overline{\rho\mathbf{V}''\mathbf{V}''}\right]$ represents the Reynolds stress work (RSW) on the mean flow, $-\nabla\cdot\left[\overline{\mathbf{F}}\cdot\langle\mathbf{V}\rangle\right]$ is the molecular stress effect on the mean flow (MSM), $C\left(\overline{\rho}k_m,\overline{\rho k_t}\right)$ denotes the energy conversion between $k_m$ and $k_t$ (CKMT), $C(\overline{\rho}k_m,\overline{\rho}e_m)$ represents the baroclinic energy conversion between $k_m$ and $e_m$ (BCM), $D(\overline{\rho}k_m)$ is the molecular dissipation of $k_m$ (MDM), $-\nabla\cdot[\overline{\rho}\langle\mathbf{V}\rangle e_m]$ stands for the mean transport of $e_m$ (MTEM), $-\nabla\left[\langle T\rangle\eta_m\frac{c_p}{\langle\theta\rangle}\cdot\overline{\rho\mathbf{V}''\theta''}\right]$ represents the effects on the mean flow resulting from the eddy transport of heat (ETH), $-\nabla\cdot[(\overline{p}-p_R)\langle\mathbf{V}\rangle]$ represents

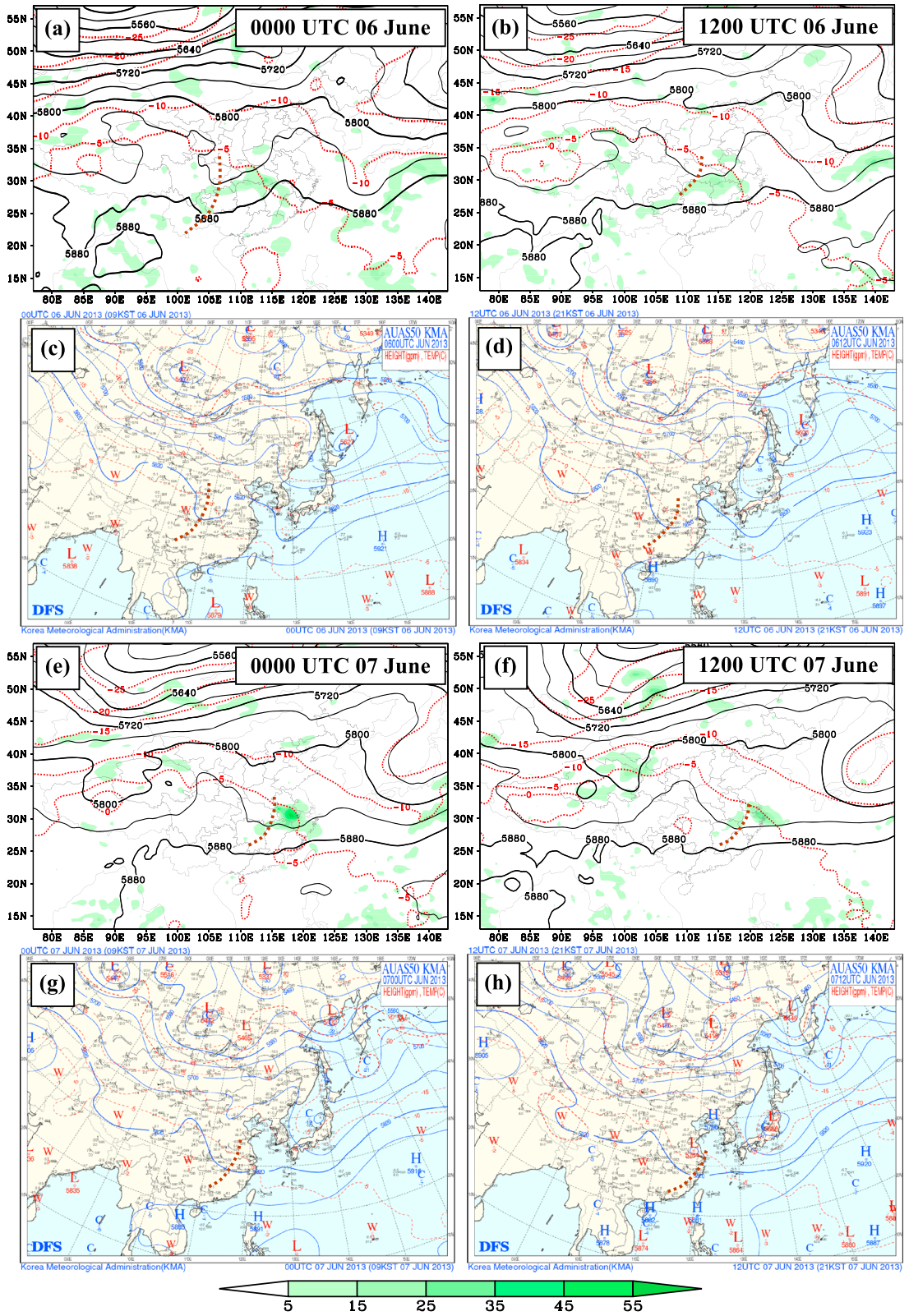


**Figure 2.** (a, b, e, and f) Simulated geopotential height (black solid lines, units: gpm), temperature (red dashed lines, units: °C), and ascending motions (shaded, units: cm $s^{-1}$) at 500 hPa. (c, d, g, and h) The weather charts from the Korea Meteorological Administration illustrating the observed geopotential height (blue solid lines, units: gpm) and temperature (red dashed, units: °C) at 500 hPa. The thick brown dotted lines represent the influencing trough line.

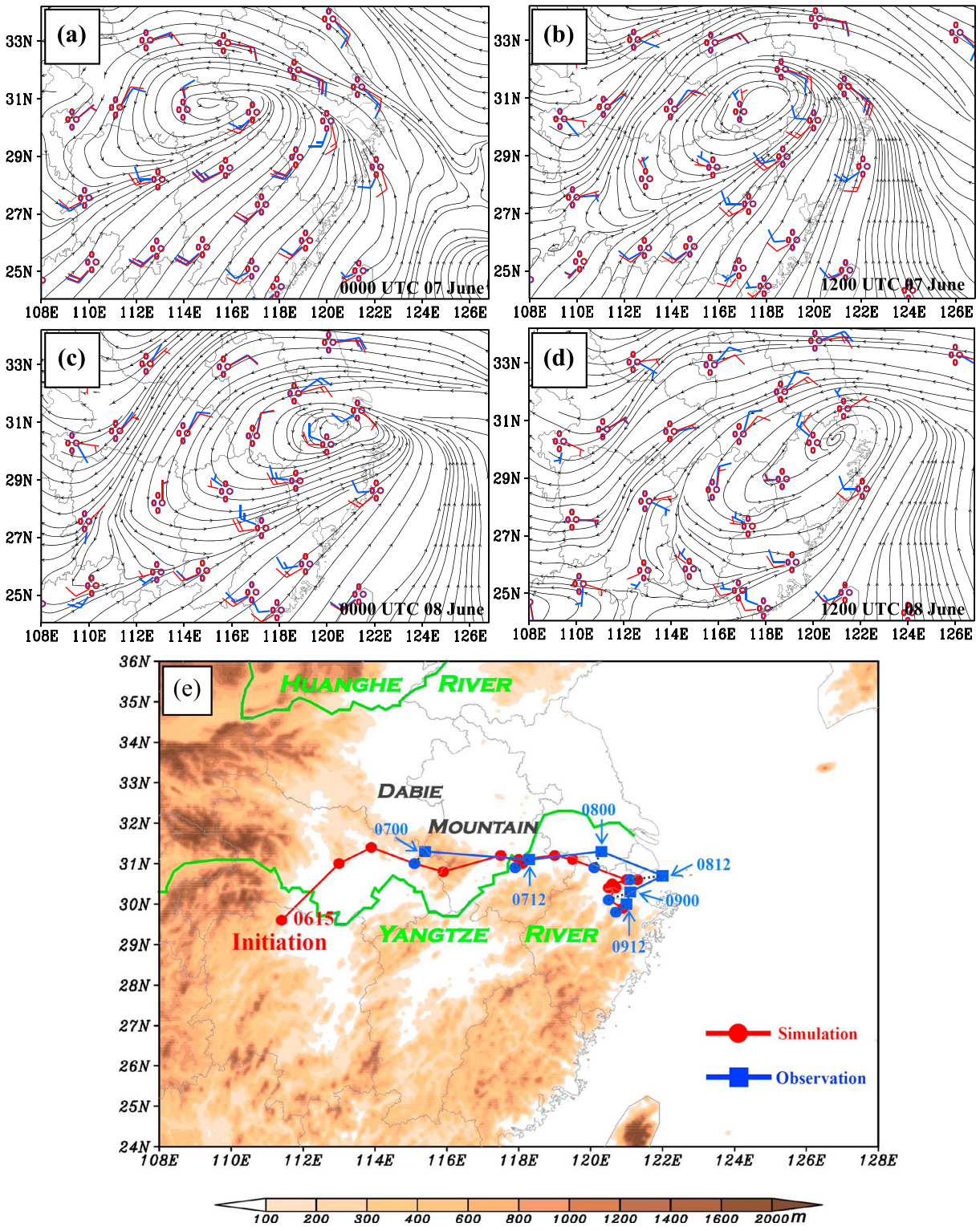


**Figure 3.** (a–d) The 850 hPa simulated wind field (red wind barb, units: m $s^{-1}$, with a full bar representing 10 m $s^{-1}$) and streamline field, as well as the observed 850 hPa wind field (blue wind barb). (e) Simulated 3-hourly vortex track (red line with circles) and 12-hourly observed track (blue line with rectangles), where the shaded is the terrain (units: m); the blue circles and rectangles connected by grey dashed lines represent the location at the same time.

the work of the mean pressure (WMP), $C(\overline{\rho}e_m, \overline{\rho e_t})$ is the conversion between $e_m$ and $e_t$ (CEMT), $G(\overline{\rho}e_m)$ denotes the generation of $e_m$ (GEM) due to diabatic processes, $-\nabla\cdot\left(\overline{\rho\mathbf{V}k_t}\right)$ represents the transport of $k_t$ (TKT), $-\nabla\cdot\left(\overline{\mathbf{F}\cdot\mathbf{V}''}\right)$ is the molecular stress effect on the eddy flow (MSE), $C\left(\overline{\rho k_t}, \overline{\rho e_t}\right)$ denotes the baroclinic energy conversion of the eddy flow (BCE), $D\left(\overline{\rho k_t}\right)$ is the molecular dissipation of $k_t$ (MDE), $-\nabla\cdot\left(\overline{\rho\mathbf{V}e_t}\right)$ represents the transport of $e_t$ (TET), $-\nabla\left(\overline{p'\mathbf{V}''}\right)$ denotes the work from the perturbation pressure (WPP), and $G(\overline{\rho e_t})$ denotes the generation of $e_t$ (GET) due to diabatic processes (Table 1).

As shown in equations (2)–(5), both the Reynolds stress work and the eddy heat transport effect can represent the eddy flow's effects on the mean flow. Terms CKMT and CEMT can represent the direct interactions (i.e., upscaled or downscaled energy cascade processes) between the mean flow and the eddy flow. Terms TKT and TET can be further decomposed into the transport effects of the mean flow and the eddy flow, respectively, and thus can partly reflect the mean flow's effects on the eddy flow. These terms are discussed in detail in section 5 to reveal the interactions between the vortex-related eddy flow and its BCs. Term CKMT can be decomposed as

$$C\left(\overline{\rho}k_m, \overline{\rho k_t}\right) = -\left(\overline{\rho\mathbf{V}''\mathbf{V}''}:\nabla\langle\mathbf{V}\rangle\right) = -\Big\{\underbrace{\overline{\rho u''u''}\frac{\partial}{\partial x}\langle u\rangle}_{\text{KP1}} + \underbrace{\overline{\rho u''v''}\frac{\partial}{\partial y}\langle u\rangle}_{\text{KP2}} + \underbrace{\overline{\rho u''w''}\frac{\partial}{\partial z}\langle u\rangle}_{\text{KP3}} +$$

$$\underbrace{\overline{\rho v''u''}\frac{\partial}{\partial x}\langle v\rangle}_{\text{KP4}} + \underbrace{\overline{\rho v''v''}\frac{\partial}{\partial y}\langle v\rangle}_{\text{KP5}} + \underbrace{\overline{\rho v''w''}\frac{\partial}{\partial z}\langle v\rangle}_{\text{KP6}} + \underbrace{\overline{\rho w''u''}\frac{\partial}{\partial x}\langle w\rangle}_{\text{KP7}} + \underbrace{\overline{\rho w''v''}\frac{\partial}{\partial y}\langle w\rangle}_{\text{KP8}} + \underbrace{\overline{\rho w''w''}\frac{\partial}{\partial z}\langle w\rangle}_{\text{KP9}}\Big\}$$

Similarly, the term CEMT can be decomposed as

$$C(\overline{\rho}e_m, \overline{\rho e_t}) = \underbrace{-\overline{\rho\mathbf{V}_h''\theta''}\cdot\frac{g^2}{\langle\theta\rangle^2}\frac{1}{N_R^2}\nabla_h\langle\theta\rangle}_{\text{EP1}} \underbrace{-\overline{\rho w''\theta''}\cdot\frac{g}{\langle\theta\rangle}\left(\frac{N_m^2-N_R^2}{N_R^2}\right)}_{\text{EP2}} \underbrace{-\overline{\rho\mathbf{V}_h''\theta''}\cdot\frac{1}{\langle\theta\rangle\rho_R}\nabla_h\overline{p}}_{\text{EP3}}$$

where $g$ is the acceleration due to gravity and $N_R$ and $N_m$ represent the reference and mean Brunt–Väisälä frequency, respectively. Additionally, in this study, for each of the budget equations (1)–(5), the sum of all the right-hand side terms except for the friction-related terms is defined as the corresponding total (TOT) term.

## 3. Overview of the Long-Lived Mesoscale Vortex and Its Geometric Characteristics

A mesoscale vortex that formed at 15:00 UTC on 06 June 2013 and lasted for about 69 h was selected for this study. This vortex was selected because it was long-lived and caused several extremely heavy rainfall events that affected a wide part of the Yangtze River Basin. These had a maximum 6-hourly precipitation of 176 mm which resulted in severe flash floods, landslides, and urban waterlogging. In addition, this case is also suitable for the main purpose of this study, because the interactions among systems of different scales are more significant for events with longer lifetimes.

### 3.1. Simulation Validation

The simulated geopotential height and temperature field at 500 hPa, and the corresponding weather charts from the Korea Meteorological Administration, are shown in Figure 2. Before the vortex was formed, a baroclinic shortwave trough appeared over Sichuan Basin (brown dotted line in Figure 2c). A small weak temperature ridge was superposed on this trough, which favored enhancement of the shortwave trough through cold temperature advection around the trough base. The simulation successfully reproduced the shortwave trough at 500 hPa (Figure 2a) and also captured the main characteristics of the temperature field. During the lifetime of the vortex, the 500 hPa trough moved eastward and increased in size. The simulation also reproduced the intensity and variation of the shortwave trough reasonably well (Figure 2). In addition, although there were differences between the simulated and observed temperature fields, overall, the simulation reasonably accounted for the main features of the temperature observations.

Figures 3a–3d show the simulated stream field/wind field and the corresponding observed wind field at 850 hPa, from which it is clear that the simulation captured reasonably well the main circulation features (including direction and intensity) associated with the mesoscale vortex. However, it should also be noted that within the central region of the vortex, the simulated wind direction obviously differed from the

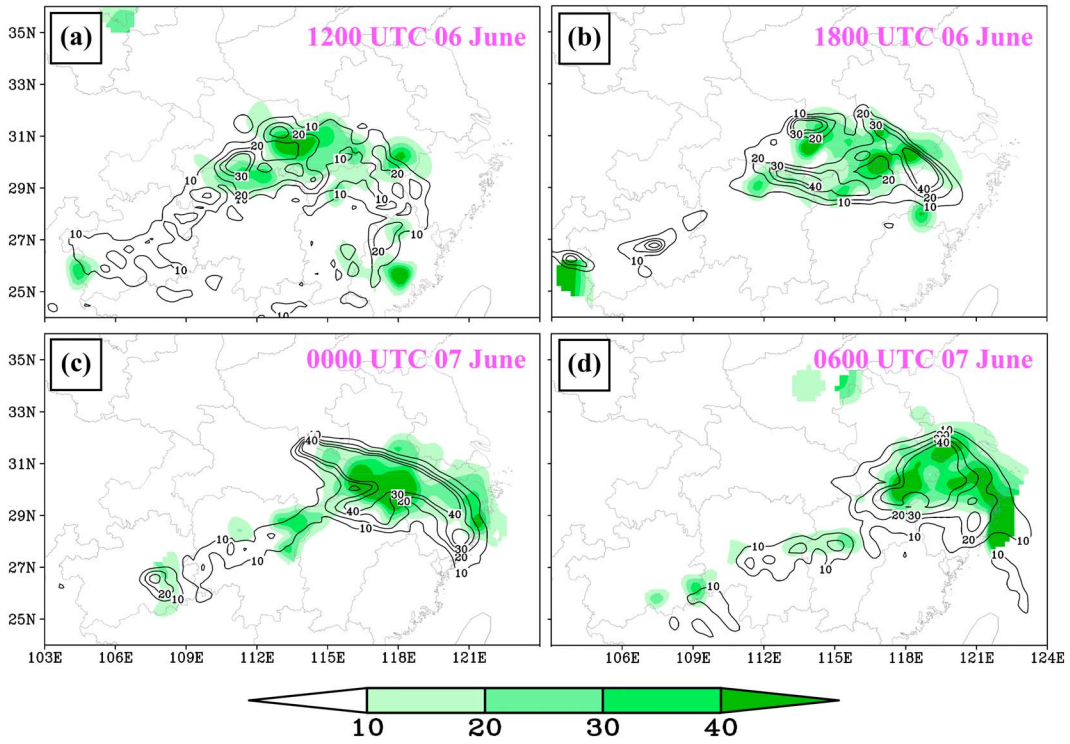


**Figure 4.** The observed 6-hourly precipitation (shaded, units: mm) and the simulated 6-hourly precipitation (black solid, units: mm) during the strong precipitation period.

observation at the station around (31.5°N, 121.5°E) (Figures 3c and 3d). This is largely because the simulated vortex track deviates from the observed one (in fact, this is inevitable for almost all vortex-related simulations). As Figure 3e illustrates, generally, displacement of the simulated vortex is in good accordance with the observations (including moving direction and speed). The maximum distance between the simulated and observed vortex centers is ~100 km (at 12:00 UTC on 08 June), which is ~13% of the vortex size at that time. In addition, the simulated vortex has very similar vertical structure features (including maximum vertical extent and evolution) to those shown by the observations (not shown).

The 6-hourly accumulated precipitation during the heavy rainfall period of the vortex is shown in Figure 4. This suggests that although the simulation may overestimate precipitation to the southwest of the vortex, and the simulated precipitation center may deviate from the observed center, overall, the simulated precipitation agrees well with the observation (the threat scores of the light to heavy rain group and the torrential rain group were 0.712 and 0.442, respectively), verifying that the simulation captures the main features of the rainfall events.

In summary, although there are differences between the simulation and the observation, the model output has reproduced the vortex's primary characteristics reasonably well.

### 3.2. Geometric Characteristics of the Mesoscale Vortex

In this study, the maximum vorticity levels associated with the vortex were mainly located at the layer of 925–850 hPa. Thus, this vertical range was used to calculate the geometry parameters using the method from *Rudeva and Gulev* [2007]. The geometry parameters at these vertical levels were averaged to represent the vortex's horizontal geometry (Figures 5 and 6). The results show that these calculated vortex outlines (Figure 5) successfully capture the primary geometric characteristics of the vortex (including range, orientation, and shape). According to the intensity, vertical stretching, divergence, and precipitation of the vortex (Figure 7), four typical stages were defined: (i) the developing stage (DVS; 15:00 UTC on 06 June to 06:00 UTC on 07 June), (ii) the early maintaining stage (EMS; 06:00 UTC on 07 June to 06:00 UTC on 08 June), (iii) the late maintaining stage (LMS; 06:00 UTC on 08 June to 06:00 UTC on 09 June), and (iv) the decaying stage (DCS; 06:00 UTC on 09 June to 12:00 UTC on 09 June).

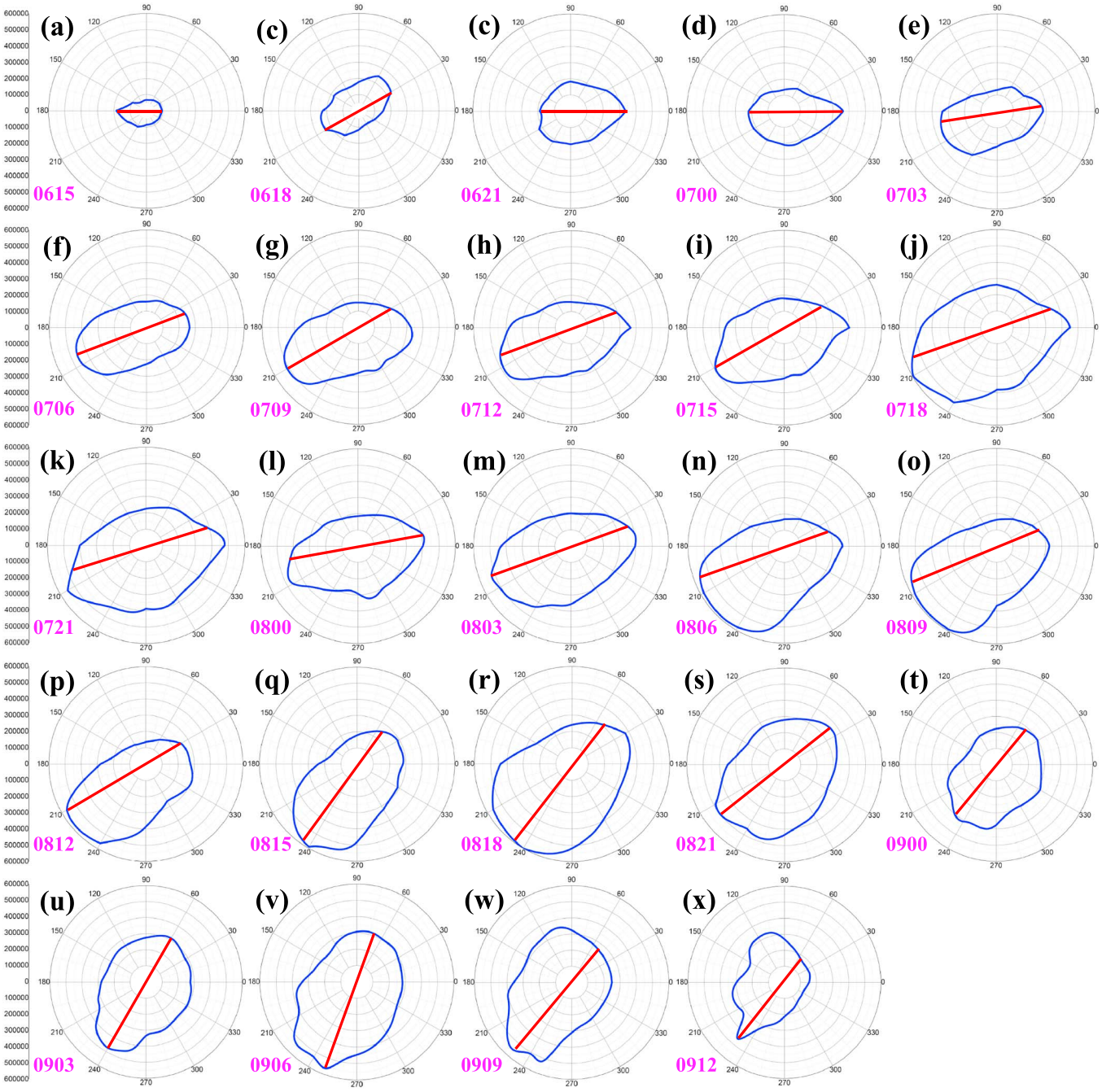


**Figure 5.** The outline of the vortex (blue closed curve) and its long axis (red solid line) during the vortex's lifetime.

As Figure 3e illustrates, at 15:00 UTC on 06 June 2013, a mesoscale vortex initiated over the middle reaches of the Yangtze River, which had a significant positive vorticity center above $3 \times 10^{-4}\,s^{-1}$ and a notable geopotential height center below 1430 gpm (not shown). The vortex was mainly orientated in the west-east direction (Figure 5a) and covered a small region: its long axis was ~250 km, the effective radius was ~100 km (Figure 6a), and its asymmetry was ~1.86 (Figure 6b). The top and bottom levels of the vortex were around 750 hPa and 950 hPa, respectively (Figure 7a). Below 850 hPa, the vortex had strong positive vorticity and $k_t$ (Figures 7a and 7b), implying that the vortex was in a rapidly developing stage. From Figure 7a, it can be observed that strong convergence occurred below 850 hPa and divergence appeared above this value. This configuration was conducive to the sustainment of ascending motions (Figure 7a).

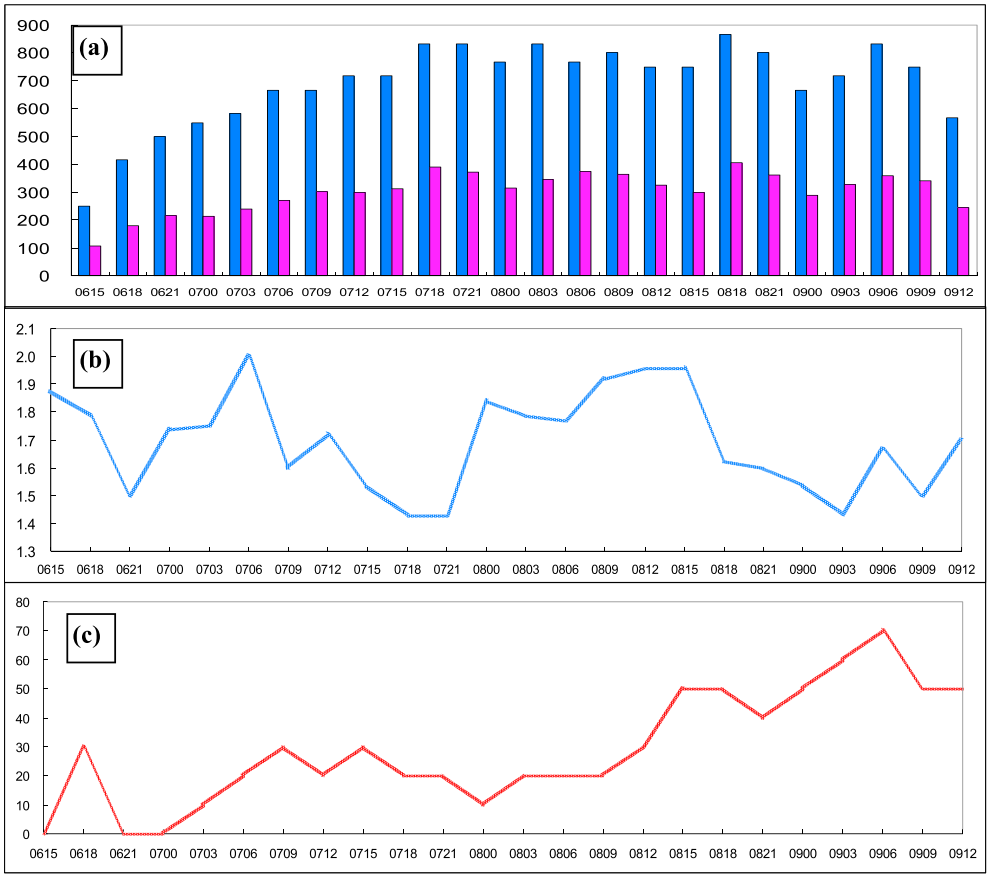


**Figure 6.** (a) The long axis (blue bar, units: km) and the effective radius (purple bar, units: km) of the vortex. (b) The asymmetry of the vortex. (c) The angle between the long axis and the easterly direction (units: deg).

Correspondingly, torrential rainfall occurred, with the maximum precipitation mainly located within quadrant 1 (Q1) of the vortex (Figure 7c).

During the DVS, the vortex mainly moved northeastward (Figure 3e), with an enlarging range (Figures 6a). From Table 2, it is evident that the vortex had a large asymmetry and the mean moving direction of the vortex (relative to the east) was very close to the vortex's long-axis orientation (i.e., the angle of the vortex's long axis relative to the east direction). As Table 2 shows, these angles were 15° and 10°, respectively. In this stage, cyclonic vorticity and $k_t$ associated with the vortex intensified rapidly and extended upward, corresponding to the development and upward stretching process of the vortex (Figures 7a and 7b). Strong cyclonic vorticity and $k_t$ regions were mainly located below 750 hPa, implying that the vortex was strong at lower levels. The vortex converged intensely below 850 hPa and diverged obviously above 550 hPa (Figure 7a). Correspondingly, ascending motions were strong and the precipitation was heavy (Figure 7c and Table 2).

During the EMS, the vortex mainly moved eastward (Figure 3e) and its speed slowed compared to that in the DVS. The mean effective radius and long-axis orientation of the vortex increased significantly, whereas the asymmetry generally decreased (Table 2). The vortex extended upward to its maximum height around 500 hPa at 12:00 UTC on 07 June, whereas from 03:00 UTC on 08 June, the vortex began to shrink vertically, which was consistent with the rapid vertical shrinking processes of the vortex-averaged vorticity and $k_t$ (Figures 7a and 7b). In this stage, overall, the vortex mean vorticity decreased significantly (Figure 7a), whereas $k_t$ still remained strong (Figure 7b). In addition, the convergence associated with the vortex weakened, with the nondivergent level mainly located around 700 hPa (Figure 7a). Correspondingly, ascending motions associated with the vortex weakened and vortex-related precipitation also decreased significantly (Table 2 and Figure 7c).

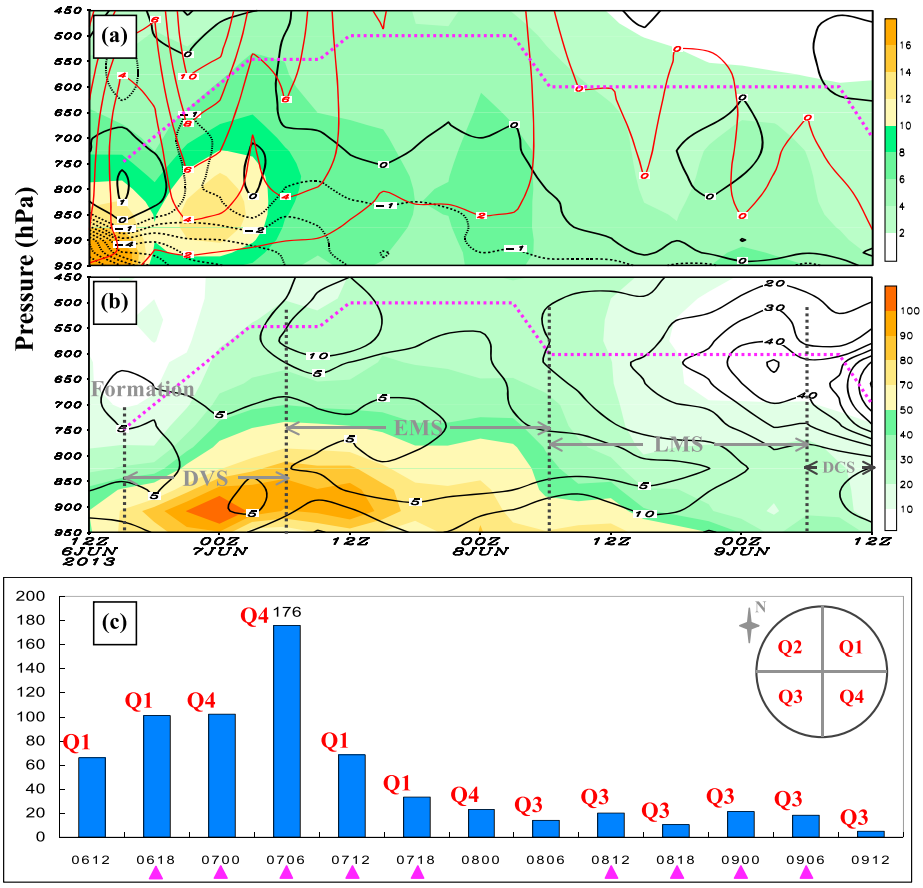


**Figure 7.** (a) The vortex-averaged vorticity (shaded, units: $10^{-5}$ s$^{-1}$), divergence (black lines, units: $10^{-5}$ s$^{-1}$), and vertical motions (red lines, units: cm s$^{-1}$). (b) The vortex-averaged $k_t$ (shaded, units: J m$^{-3}$) and $e_t$ (black lines, units: J m$^{-3}$), where the dotted purple line represents the top level of the vortex and the grey dashed lines mark the typical stages of the vortex as follows: the DVS, EMS, LMS, and DCS. (c) The observed maximum 6-hourly precipitation associated with the vortex (units: mm) and the quadrant is located in Q1–Q4, where the purple rectangles mark the typical stage.

**Table 2.** Typical Stage-Averaged Precipitation (Units: mm), Effective Radius (Units: km), Top Vertical Level (Units: hPa), Asymmetry, Long-Axis Orientation/Moving Direction (Units: Deg), and Energy Budget Terms Averaged at Heights of 1000 m and 1500 m Within the Key Area During the Stages (Units: $10^{-5}$ W m$^{-3}$)

| | DVS | EMS | LMS | DCS |
|---|---|---|---|---|
| Precipitation | 108 | 54.8 | 16.8 | 9.3 |
| Effective radius | 204 | 330 | 345 | 304 |
| Top level | 642 | 516 | 600 | 634 |
| Asymmetry | 1.78 | 1.68 | 1.71 | 1.61 |
| Angles | 10/15 | 21/9 | 43/56 | 57/80 |
| TOT ($k_t$) | 90.6 | 34.1 | −8.3 | −4.1 |
| TKT | −34.4 | −88.2 | −30.9 | 3.9 |
| BCE | 75.2 | 86.5 | 7.4 | 3.2 |
| CKMT | 49.8 | 35.8 | 15.2 | −11.2 |
| KP2 | 21.1 | 20.5 | 12.6 | −5.1 |
| KP5 | 42.8 | 38.4 | 15.3 | −12.2 |
| CEMT | −2.8 | 11.9 | 17.9 | 16.8 |
| EP1 | 3.0 | 17.6 | 24.5 | 12.6 |
| EP2 | −5.6 | −5.5 | −6.3 | 4.5 |

In the LMS, the vortex primarily maintained quasi-stationary behavior (Figure 3e). Its mean effective radius was maximized in this stage (Table 2), whereas the top level of the vortex decreased to 600 hPa (Figure 7a), both of which favored an increase in the horizontal divergence. During this period, both the vorticity and $k_t$ associated with the vortex decreased significantly (Figures 7a and 7b), implying that the vortex began to weaken. The convergence associated with the vortex weakened significantly, and the nondivergent level descended to 900 hPa or below. Ascending motions associated with the vortex also weakened notably (Figure 7a), and correspondingly, the precipitation decreased significantly (Table 2).

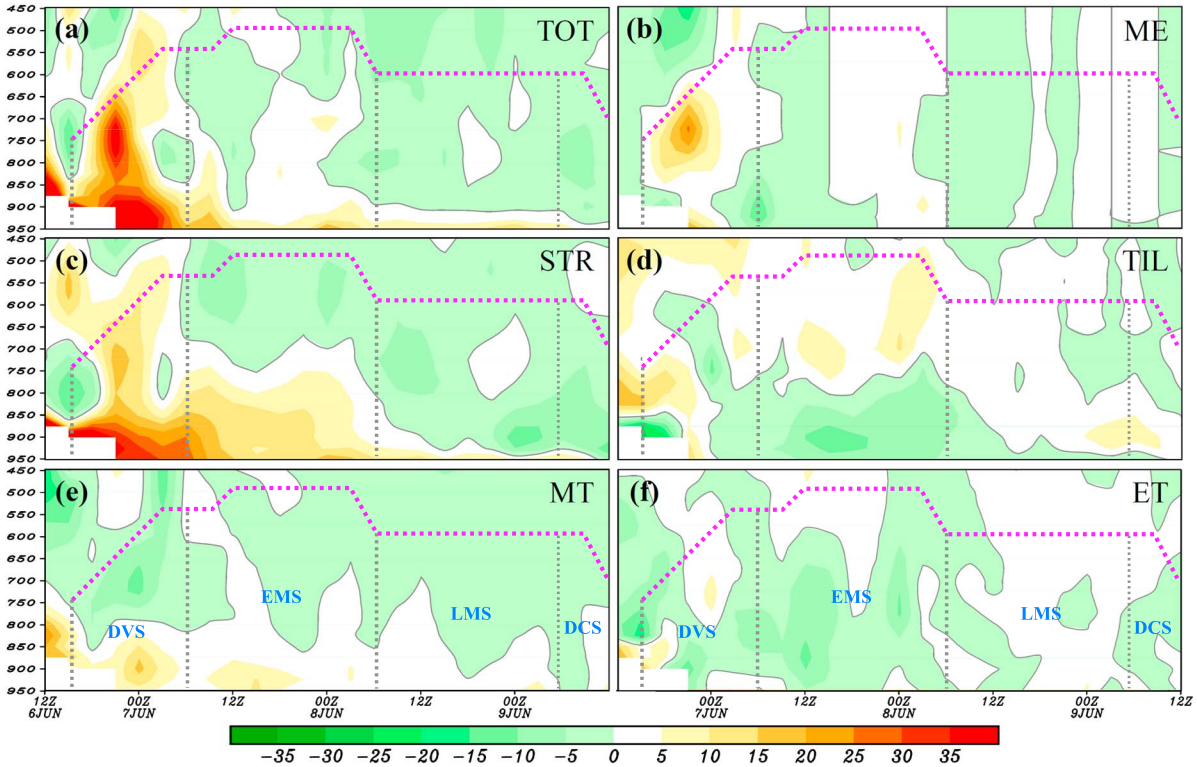


**Figure 8.** The vortex-averaged eddy flux circulation budget terms (shaded, units: $10^{-10}$ s$^{-2}$). The grey solid is the zero contour, and the dashed purple line represents the top level of the vortex: (a) total (TOT), (b) movement effect (ME), (c) stretching effects (STR), (d) tilting effect (TIL), (e) mean transport (MT), and (f) eddy transport (ET).

During the DCS, the vortex also remained quasi-stationary (Figure 3e). Its effective radius decreased (Figures 5v–5x) and the vortex top level lowered (Figure 7a), both of which indicate that the three-dimensional size of the vortex decreased. Meanwhile, the vortex-averaged vorticity and $k_t$ decreased rapidly (Figures 7a and 7b), which also indicates attenuation of the vortex. As Figure 7a shows, divergence and descending motion dominated the vortex in this stage. As a result, precipitation associated with the vortex reached a minimum (Table 2).

## 4. Mechanisms Accounting for Vortex Evolution

In this study, equation (1) was used to investigate the evolution mechanisms of the vortex and the budget was calculated using the outlines shown in Figure 5. Our results show that, although term RES was neglected, and there were other calculation uncertainties (including the accuracy of the difference scheme and the time resolution), the overall balance of the budget was reasonably good (not shown) and thus can be used for further analysis.

During the DVS, a strong positive TOT dominated the mesoscale vortex (Figure 8a), implying that the vortex rapidly intensified. Below 800 hPa, shrinking effects (term STR) (Figure 8c) associated with strong convergence (Figure 7a) dominated the vortex development and BC transport (term MT) also favored enhancement of the vortex (Figure 8e). In contrast, the tilting effects (term TIL) and the eddy transport (term ET) mainly slowed the development of the vortex (Figures 8d and 8f). Above 800 hPa, shrinking effects associated with convergence (Figures 7a and 8a) and the effects related to vortex movement (term ME) dominated vortex development and upward stretching processes (Figure 8b). In addition, the tilting effects mainly favored the development process (Figure 8d) and BC transport was the strongest effect acting against vortex intensification (Figure 8e).

During the EMS, overall, a positive TOT dominated the vortex, particularly in the lower troposphere (Figure 8a). This implies that the conditions were generally conducive for sustaining the vortex. Below 700 hPa, shrinking

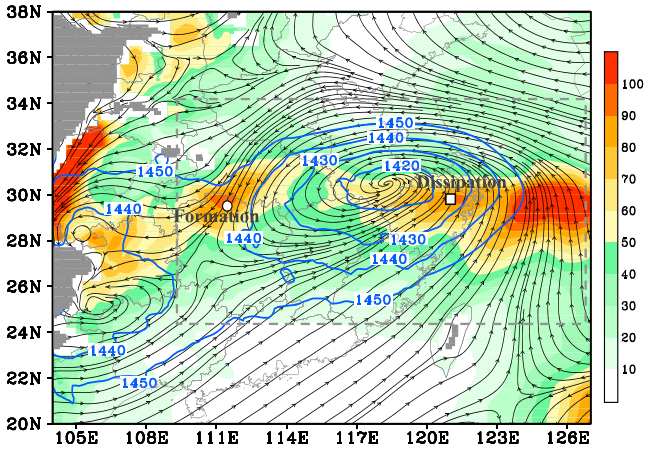


**Figure 9.** The time-averaged stream field, geopotential height (blue solid, units: gpm), and $k_t$ (shaded, units: J m$^{-3}$) at 850 hPa during the entire vortex lifetime, where the open circle represents the formation location of the vortex, the open rectangle represents the dissipation location of the vortex, and the large dashed rectangle outlines the key area of the vortex.

effects associated with convergence (Figures 7a and 8c) dominated vortex maintenance and BC transport was also favorable to vortex maintenance (Figure 8e). In contrast, the tilting and eddy transport effects were detrimental to vortex sustainment (Figures 8d and 8f). Above 700 hPa, the tilting effect was the most favorable factor for vortex maintenance (Figure 8d), whereas the stretching effects associated with divergence (Figures 7a and 8c) and the BC transport (Figure 8e) mostly had the opposite effect. From Figure 8b, it can be seen that, overall, movement was mainly detrimental for vortex sustainment before 15:00 UTC on 07 June, whereas the opposite was true later on. The discussion of *Fu and Sun* [2012] demonstrated that the configuration of the vortex displacement relative to the vorticity pattern of the BCs was vital in determining the effect of term ME. As the vortex moved from areas of low vorticity to areas of higher vorticity, the term ME favored vortex sustainment, whereas as the vortex moved from large vorticity regions to smaller ones, the opposite was true. In this study, displacement of the vortex and distribution of the vorticity also confirmed this result (not shown).

During the LMS, term TOT weakened significantly, with the favorable regions mainly being located below 900 hPa (Figure 8a). Thus, overall, the conditions were no longer conducive to vortex sustainment. Stretching effects associated with divergence (Figures 7a and 8c) and BC transport (Figure 8e) mainly accounted for the weakening of the vortex above 900 hPa, whereas the tilting effect and the eddy transport effect generally resisted the vortex attenuation (Figures 8d and 8f). In addition, the term ME (vortex movement) mainly weakened the vortex before 21:00 UTC on 08 June (Figure 8b), whereas the opposite was true later on.

During the DCS, a highly negative TOT dominated the vortex (Figure 8a), implying that the vortex weakened rapidly. Stretching effects associated with divergence (Figures 7a and 8c) were the dominant factors accounting for vortex dissipation. The transport effects of the BC and the eddy flow (terms MT and ET) also accelerated the attenuation (Figures 8e and 8f). In addition, the tilting effect mainly resisted dissipation below 800 hPa (Figure 8d) but enhanced it above 800 hPa.

## 5. Interactions Between the Vortex and Its Background Circulations

In this study, energy budgets associated with the vortex (equations (2)–(5)) were calculated within a key area (24.5–34°N, 109–127°E), defined as shown in Figure 9. This key area, within which the vortex-BC interactions mainly occurred, was determined by the whole vortex lifetime mean stream field, geopotential height, and $k_t$. The sensitivity of the key area selection was tested, and the results show that the key-area-based calculations were insensitive to relatively small changes (±90 km to each boundary of the key area). Generally, although the energy budget results suffered from neglecting the friction-related effects and the calculation uncertainties discussed in section 4, the overall balance between the tendency term on the left-hand side of the energy budget equation and the sum of the right-hand side terms (except for friction-related terms) is reasonable (not shown).

### 5.1. Energy Features and Budgets During the Developing Stage

#### 5.1.1. Perturbation Kinetic Energy

After vortex formation, a significant $k_t$ center associated with the vortex appeared in the lower troposphere (Figures 10a and 11a). Meanwhile, a strong positive TOT ($k_t$) appeared around the vortex (Figures 12a

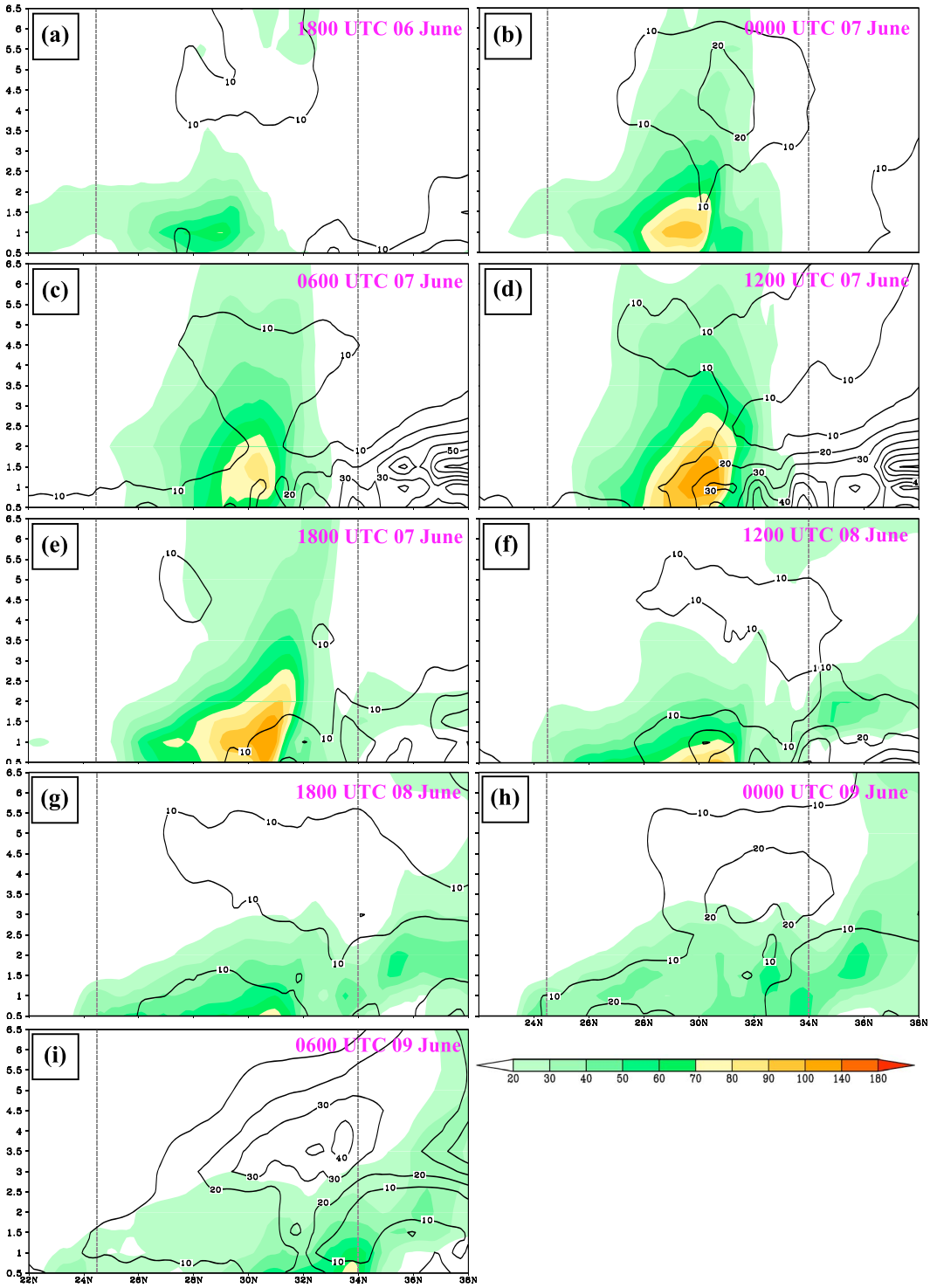


**Figure 10.** Cross sections of the zonal averaged $k_t$ (shaded, units: J m$^{-3}$) and $e_t$ (black lines, units: J m$^{-3}$) during typical stages of the vortex, where the grey solid lines mark the key area.

and 12f). This means that conditions during the DVS were favorable for rapid intensification of the vortex. As a result, this $k_t$ center intensified, stretched upward, and moved northward (Figures 10a–10c and 11a–11c), which was consistent with the vortex's enhancement, vertical extension, and northeastward displacement (Figures 3e and 7a).

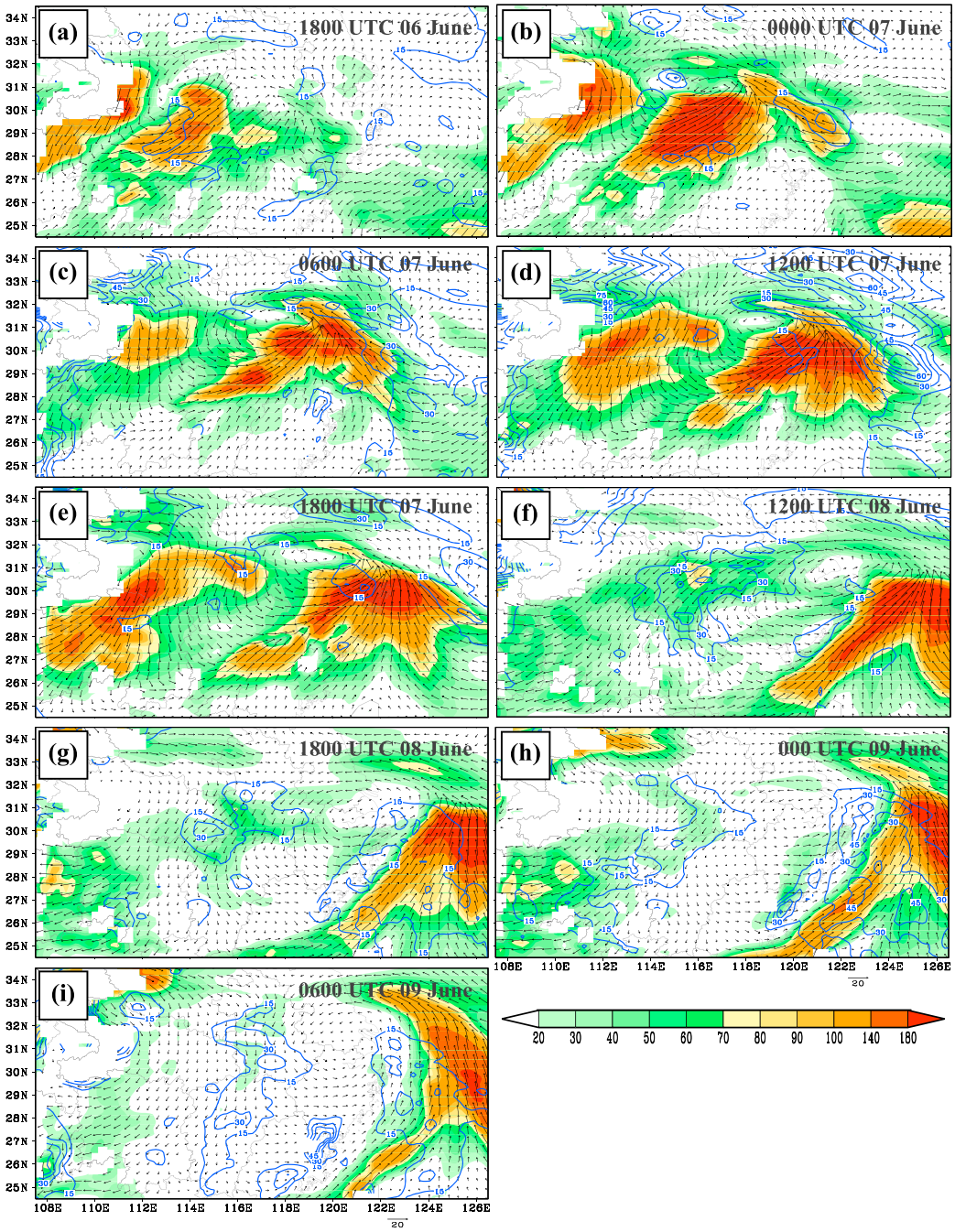


**Figure 11.** The distribution of $k_t$ (shaded, units: J m$^{-3}$), $e_t$ (blue solid lines, units: J m$^{-3}$), and perturbation horizontal wind field (vectors, units: m s$^{-1}$) at the level of 1000 m during the typical stages of the vortex.

Overall, during the DVS, the transport of $k_t$ had a negative effect at the lower levels of the key area (Table 2 and Figures 12a and 12f), such that the mean and eddy flows mainly transported $k_t$ out of the key area, making this region an energy source of $k_t$. Within the key area, a significant downscaled energy cascade of KE (CKMT $> 0$) occurred below 3 km (i.e., energy was transferred from the BCs to the vortex; see equations (2) and (4) for details) (Table 2). The energy transferred from the BC to the vortex-related eddy flow favored vortex development. As discussed in section 2.2.3, the energy cascade term CKMT can be decomposed into nine separate parts. In this case, the most important factors are KP2 $= -\overline{\rho u'' v''} \frac{\partial}{\partial y} \langle u \rangle$ and KP5 $= -\overline{\rho v'' v''} \frac{\partial}{\partial y} \langle v \rangle$ (Table 2). Physical images of

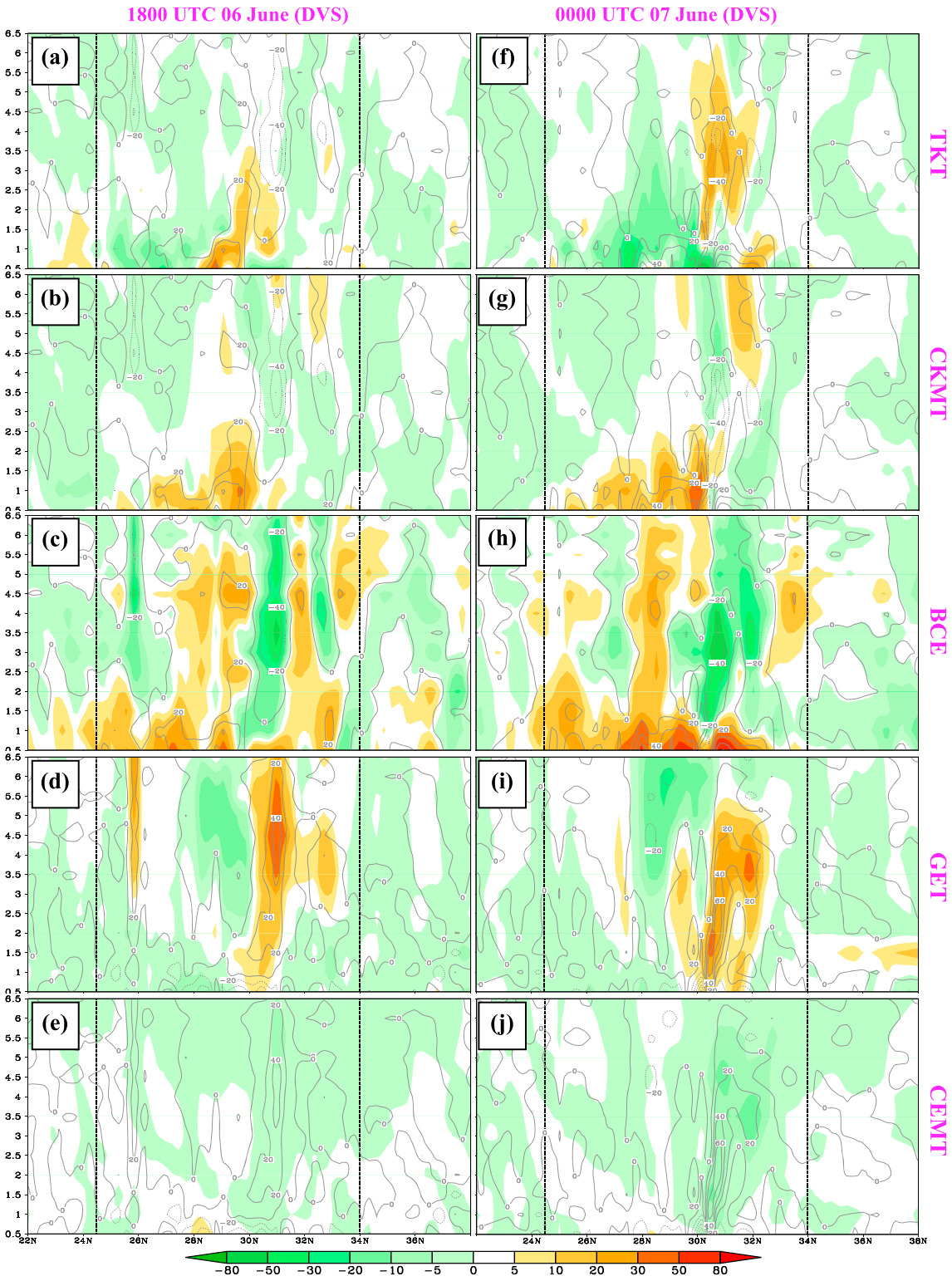


**Figure 12.** Energy budget terms (shaded) and the corresponding term TOT (grey lines) during the DVS (units: $10^{-4}$ W m$^{-3}$), where the grey solid lines mark the key area.

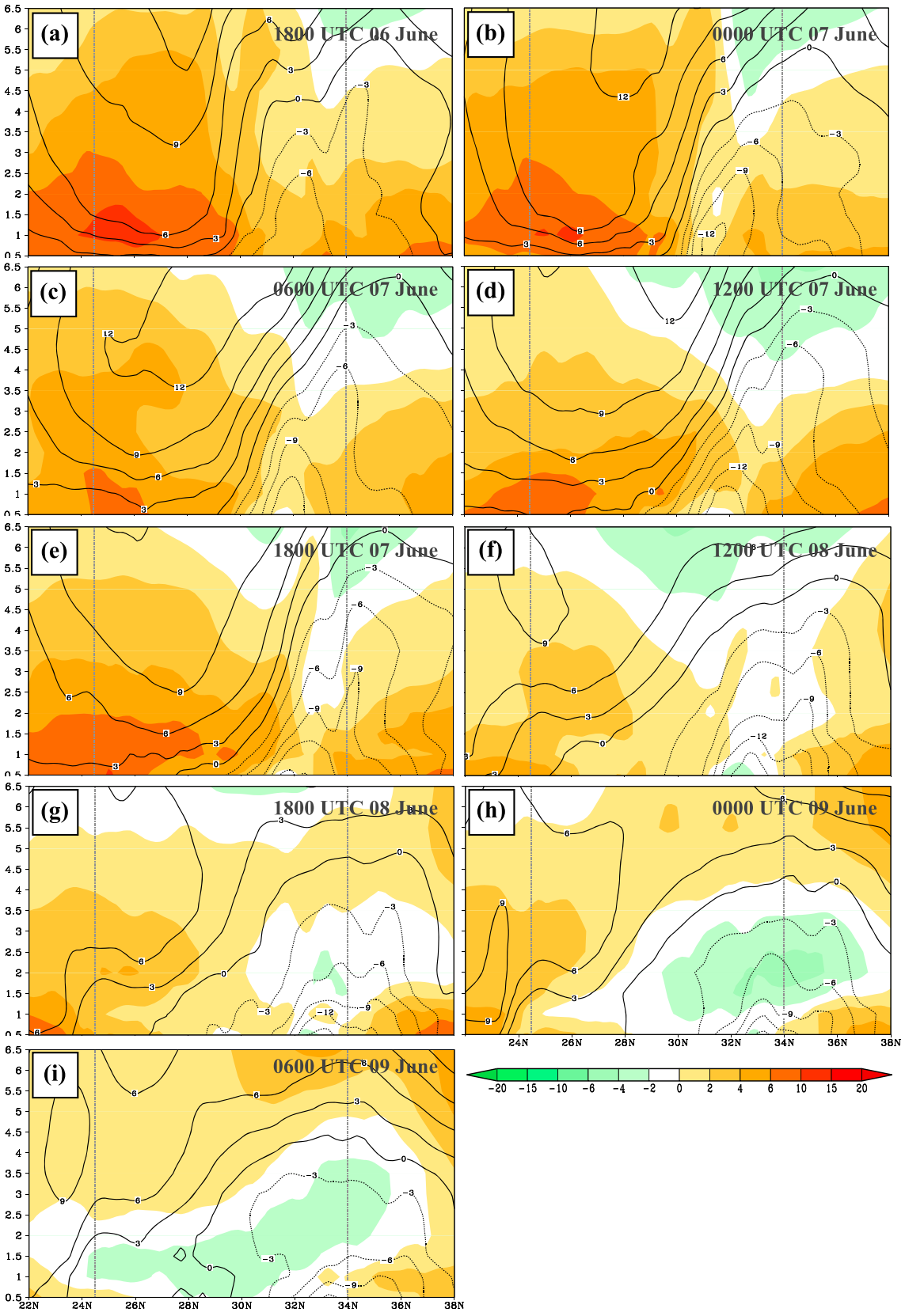


**Figure 13.** The cross section of the mean meridional wind (shaded, units: m $s^{-1}$) and mean zonal wind (black lines, units: m $s^{-1}$) during typical stages of the vortex, where the grey solid lines mark the key area.

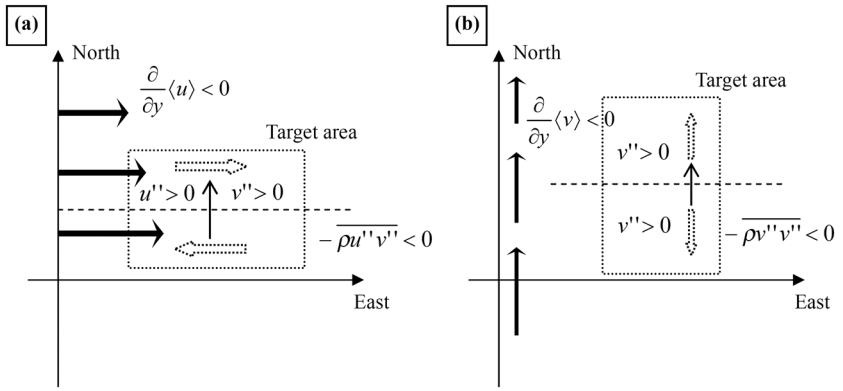


**Figure 14.** Schematic illustration of the interaction terms, where the thick solid arrows denote the mean flow, the thin solid arrows represent the transport direction, the dotted open arrows stand for the transport effects, and the dashed line is the reference line.

these two terms are shown to understand how the downscaled energy cascade of KE occurs. Figures 13a–13c show that, during the DVS, levels below 3 km generally had $\frac{\partial}{\partial y}\langle u\rangle < 0$ (cyclonic circulation) and $\frac{\partial}{\partial y}\langle v\rangle < 0$ (convergent flow) around the vortex. These features corresponded to the lower-level cyclonic shear and convergent zone within the key area (Figure 9). Meanwhile, the key area generally had $-\overline{\rho u'' v''} < 0$ below 3 km (not shown), which means that the eddy transport of the zonal perturbation momentum was mainly in the northward direction. The situation above can be represented by Figure 14a concisely. Under this configuration, zonally, the mean flow does positive work to the eddy flow within the target area, which favors enhancement of $k_t$, because $\langle u\rangle$ and $u''$ are in the same direction. Meridionally, the transport of $u''$ by $v''$ results in eastward eddy flow to the north of the reference line and westward eddy flow to the south. Thus, the eddy flow does negative work to the mean flow within the target area, which reduces $k_m$. Because the mean zonal wind decreases to the north, within the target area, the positive work (to the north of the reference line) is smaller than the negative work (to the south of the reference line). This increase of perturbation KE ($k_t$) and decrease of mean KE ($k_m$) indicate a downscaled energy cascade of KE (energy was transferred from the mean flow to the vortex-related eddy flow). Similarly, term KP5 can be explained using the schematic illustration shown in Figure 14b.

Figures 12c and 12h show that the baroclinic energy conversion (term BCE) was strong at the lower levels of the key area. It acted as the most favorable factor for vortex development (Table 2). In addition, around the vortex, the strong positive baroclinic energy conversion associated with the eddy flow could extend upward to 6.5 km, dominating the vertical enlargement of the positive $k_t$ regions (Figures 10a–10c). As reported by *Kucharski and Thorpe* [2000], the baroclinic energy conversion term BCE $= -\overline{\mathbf{V}_h''} \cdot \nabla_h p'$, denoting the perturbation pressure gradient force's work done on the eddy flow. From Figures 15a–15c, it is apparent that during the DVS, the vortex had a strong negative perturbation pressure center; thus, the perturbation pressure gradient force $-\nabla_h p'$ generally pointed inward to the vortex center. Meanwhile, the eddy flow associated with the vortex showed significant convergent features (Figures 11a–11c). Therefore, around the vortex, BCE $= -\overline{\mathbf{V}_h''} \cdot \overline{\nabla_h p'} > 0$ (Table 2); i.e., the baroclinic energy conversion favored vortex development through the perturbation pressure gradient force's positive work on the eddy flow.

### 5.1.2. Other Energies

For eddy exergy ($e_t$) within the key area, an increase was also significant during the DVS, particularly for the lower troposphere to the north of the vortex (Figures 10a–10c). Precipitation-related diabatic heating effects (term GET) were vital for the intensification of $e_t$ (Figures 12d and 12i). In contrast, a negative CEMT generally dominated the key area (Figures 12e and 12j), implying that an upscaled energy cascade of exergy occurred, which transferred energy from the eddy flow to its BCs. Compared to other terms in the $e_m$ budget (not shown), term CEMT was weak, indicating that this upscaled energy cascade only slightly affected the BCs. As discussed in section 2.2.3, CEMT contains three seperate parts. In this case, only two parts, i.e., EP1 $= -\overline{\rho \mathbf{V}_h'' \theta''} \cdot \frac{g^2}{\langle\theta\rangle^2} \frac{1}{N_R^2} \nabla_h \langle\theta\rangle$ and EP2 $= -\overline{\rho w'' \theta''} \cdot \frac{g}{\langle\theta\rangle} \left(\frac{N_m^2 - N_R^2}{N_R^2}\right)$, were important. As

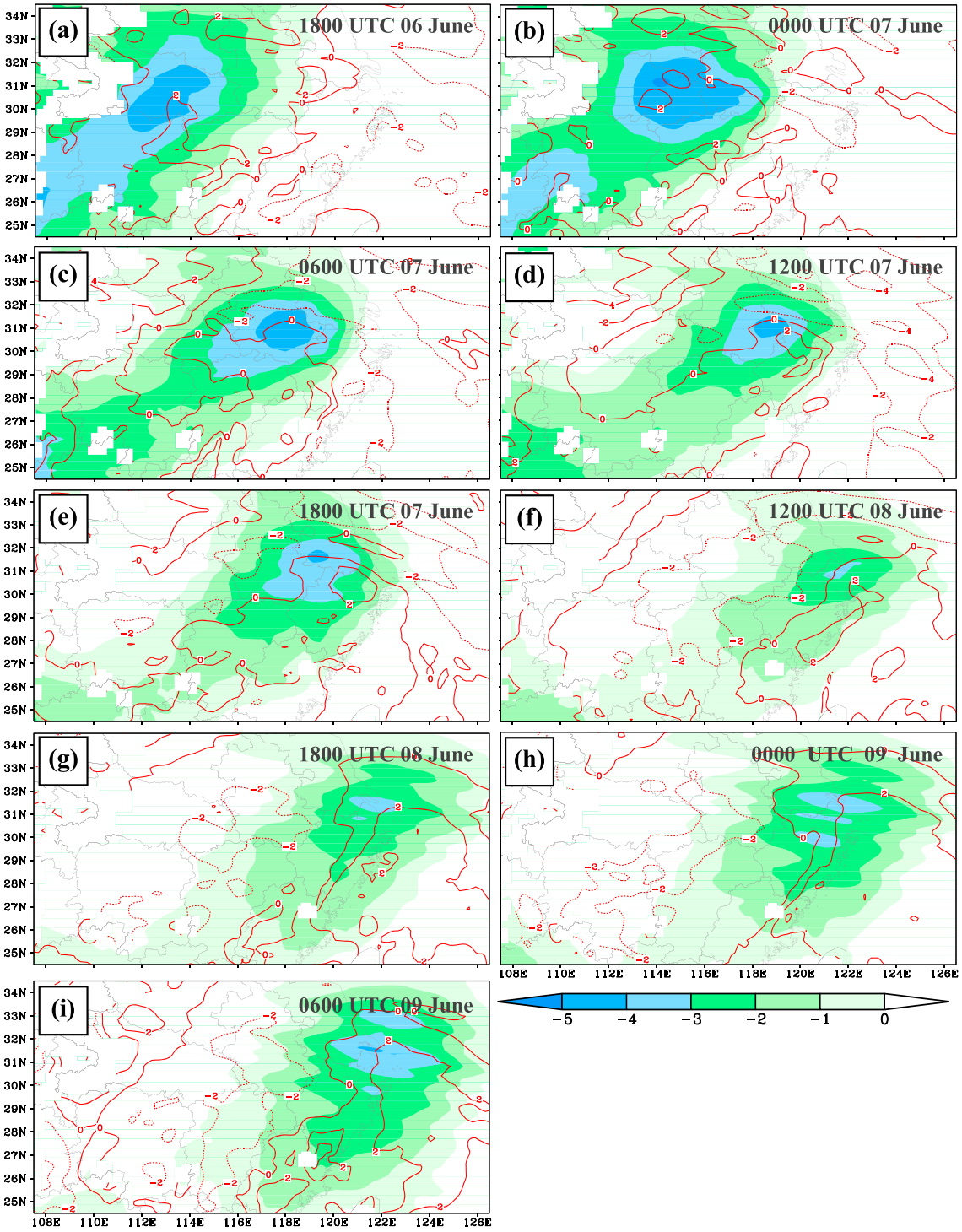


**Figure 15.** The distribution of the perturbation pressure (shaded, units: hPa) and the perturbation potential temperature (red lines, units: K) at the level of 1000 m during the typical stages of the vortex.

Table 2 shows, overall, EP2 favored the upscaled energy cascade of exergy through vertical eddy transport of heat, whereas EP1 acted conversely through the horizontal eddy heat transport. Physical images of these two terms are shown to understand how the energy cascade of exergy occurs. Largely owing to the meridional distribution of the solar radiation, at lower levels of the key area, the BCs generally warmed toward the south (Figures 16a–16c). Correspondingly, BCs within Q3 and Q4 of the vortex were warmer

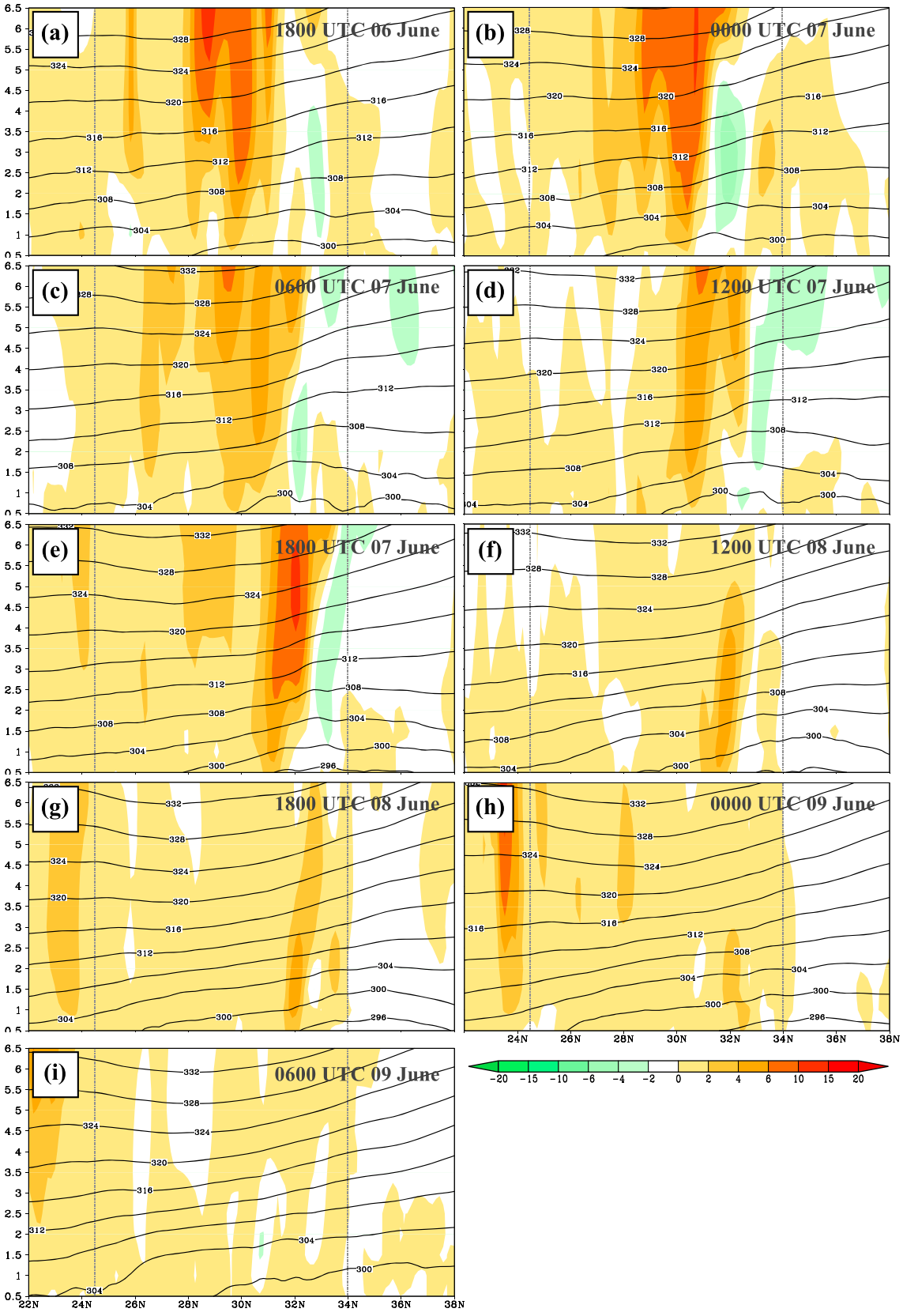


**Figure 16.** The cross section of the mean vertical wind (shaded, units: m $s^{-1}$) and mean potential temperature (black solid lines, units: K) during typical stages of the vortex, where the grey solid lines mark the key area.

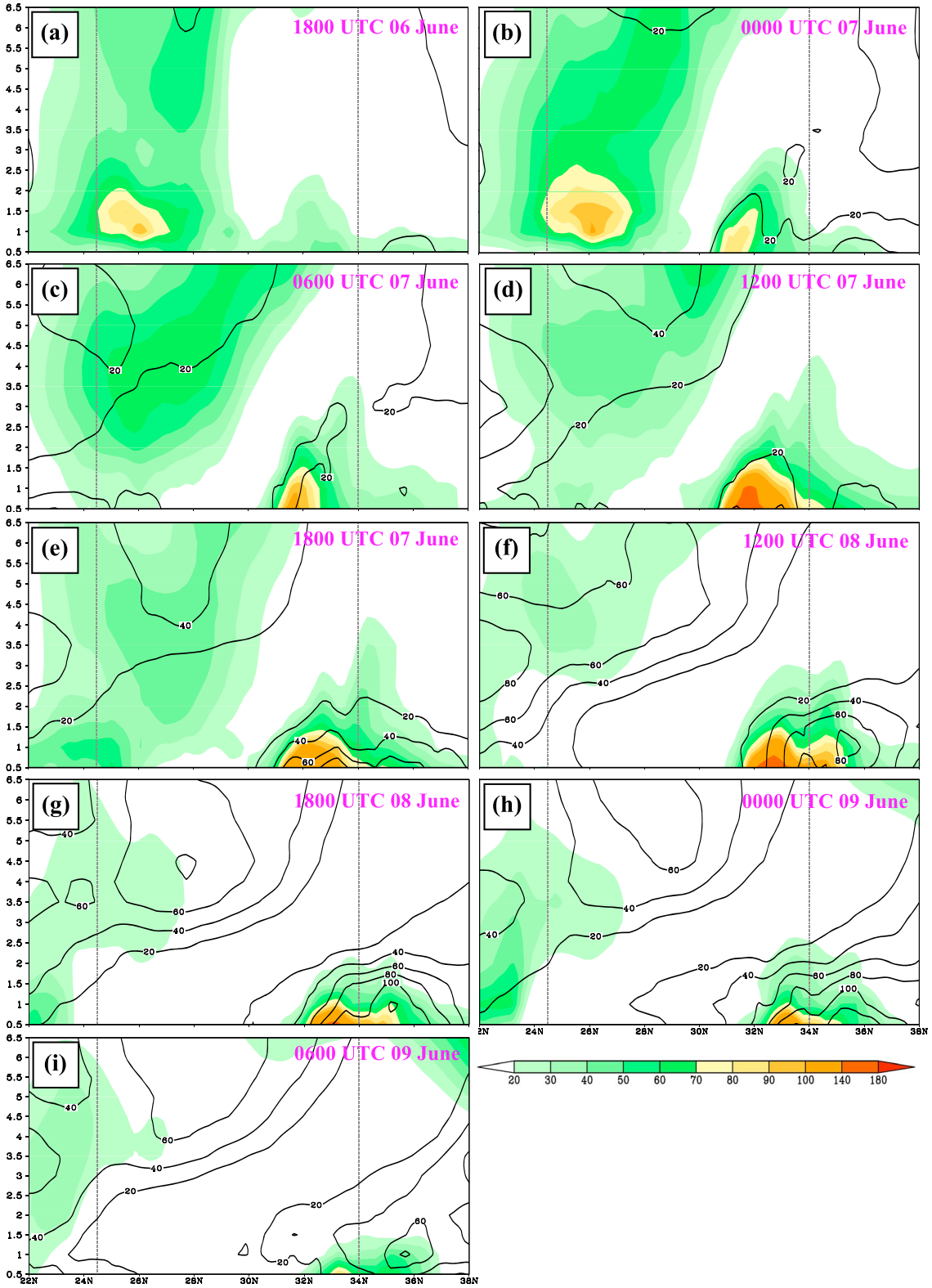


**Figure 17.** Cross sections of the zonal averaged $k_m$ (shaded, units: J m$^{-3}$) and $e_m$ (black lines, units: J m$^{-3}$) during typical stages of the vortex, where the grey solid lines mark the key area.

than within Q1 and Q2. Figure 7c demonstrates that Q4 (the vortex's southeast quadrant) had strong ascending motions and a positive $\theta''$ zone related to latent heat release (Figures 15a–15c), both of which rendered $\overline{w''\theta''} > 0$ (i.e., upward eddy heat transport). Therefore, EP2 $< 0$ (in this case, other components in EP2 are positive); i.e., upward eddy heat transport in warm regions (Q4) made this area warmer. Thus, the horizontal temperature gradient (baroclinity/exergy) of the BCs was enhanced. This was corresponding to the upscaled energy cascade of exergy. As Figures 16a–16c show, corresponding to the basic thermodynamical pattern of BCs, $-\nabla_h\langle\theta\rangle$ mainly pointed northward. Meanwhile, around the vortex, term $\overline{\rho\mathbf{V}_h''\theta''}$ (i.e., horizontal eddy heat transport) also predominantly pointed northward (Figures 11a–11c and 15a–15c). Therefore, EP1 $> 0$; i.e., the horizontal eddy transport of heat mainly weakened the horizontal temperature gradient (baroclinity/exergy) of the BCs, which corresponded to a downscaled energy cascade of exergy.

From Figures 17a–17c, it can be seen that, in the lower troposphere, the $k_m$ center to the north of the vortex intensified rapidly during the DVS, mainly due to enhancement of the mean easterly wind (Figures 13a–13c). Baroclinic energy conversion from $e_m$ to $k_m$ was the dominant factor for this enhancement (not shown). In contrast, the $k_m$ center to the south of the vortex weakened, which mainly corresponded to a decrease of the mean southerly wind (Figures 13a–13c). This weakening was dominated by the Reynolds stress negative work on the mean flow (term RSW).

To the north of the vortex, $e_m$ increased (Figures 17a–17c) mainly due to the work of the mean pressure (term WMP), whereas in the southern part of the key area, $e_m$ intensified, primarily due to the diabatic heating processes associated with the precipitation (GEM $> 0$). It should be noted that, because the mean Carnot factor was generally positive at higher levels and negative below these levels (not shown), the diabatic term GEM had different effects to the mean flow at lower and higher levels.

### 5.2. Energy Features and Budgets During the Early Maintaining Stage

#### 5.2.1. Perturbation Kinetic Energy

During the EMS, within the key area, the energy conditions were generally favorable for vortex sustainment (Figures 18a and 18f), particularly for the lower levels (Table 2). Correspondingly, $k_t$ associated with the vortex remained strong (Figures 10c–10e and 11c–11e). The baroclinic energy conversion (term BCE) dominated the $k_t$ center's sustainment below 2.5 km (Table 2 and Figures 18c and 18h), whereas at the levels of 2.5–4 km, baroclinic energy conversion was mainly detrimental to the vortex's persistence. The different effects of baroclinic energy conversion at different levels were closely related to the vertical distribution of the eddy flow's divergence: levels below 2.5 km mainly featured convergence (Figures 11c–11e), where the perturbation pressure gradient force did positive work on the eddy flow (BCE $> 0$), whereas levels of 2.5–4 km generally had divergence (Figure 7a), and thus, negative work appeared.

From Figures 18b and 18g, it can be seen that, around the vortex, the downscaled energy cascade of KE still remained strong, which favored the maintenance and upward extension of the vortex (Figure 7b). The lower-level cyclonic shear and convergent zone (Figure 9) sustained the strong meridional gradients of the BC wind field (Figures 13c–13e), which provided favorable conditions for the energy cascade processes.

At lower levels of the key area, the mean and eddy flows mainly transported $k_t$ out of the key area (Table 2), which was detrimental to the vortex's persistence. In contrast, it should be noted that, at the level of 1–5 km, within the northern quadrants of the vortex, a strong convergence of $k_t$ (TKT $> 0$) appeared (Figures 18a and 18f), which favored upward extension and northward growth of the vortex (Figure 7b).

#### 5.2.2. Other Energies

During the EMS, lower levels of the key area mainly had strong $e_t$ (Figures 11c–11e). The diabatic heating effect associated with precipitation generally favored the persistence of $e_t$ (Figure 18d). Below 2.5 km, an upscaled energy cascade of exergy (CEMT $< 0$) dominated the key area before 18:00 UTC on 07 June (Figures 18e and 18j), mainly due to the upward eddy transport of heat (not shown), which enhanced the baroclinity of the BCs. After 18:00 UTC on 07 June, a downscaled energy cascade of exergy appeared (Table 2), mainly due to the northward eddy transport of heat that weakened the baroclinity of the BCs.

Figures 13c–13e show that the mean easterly wind center to the north of the vortex remained strong during the EMS. Correspondingly, $k_m$ remained strong to the north of the vortex (Figures 17c–17e). The baroclinic energy conversion (BCM $= \langle\mathbf{V}_h\rangle \cdot \nabla_h\overline{p}$), which was largely determined by the westward mean pressure gradient force's positive work on the mean easterly wind (not shown), was the dominant factor

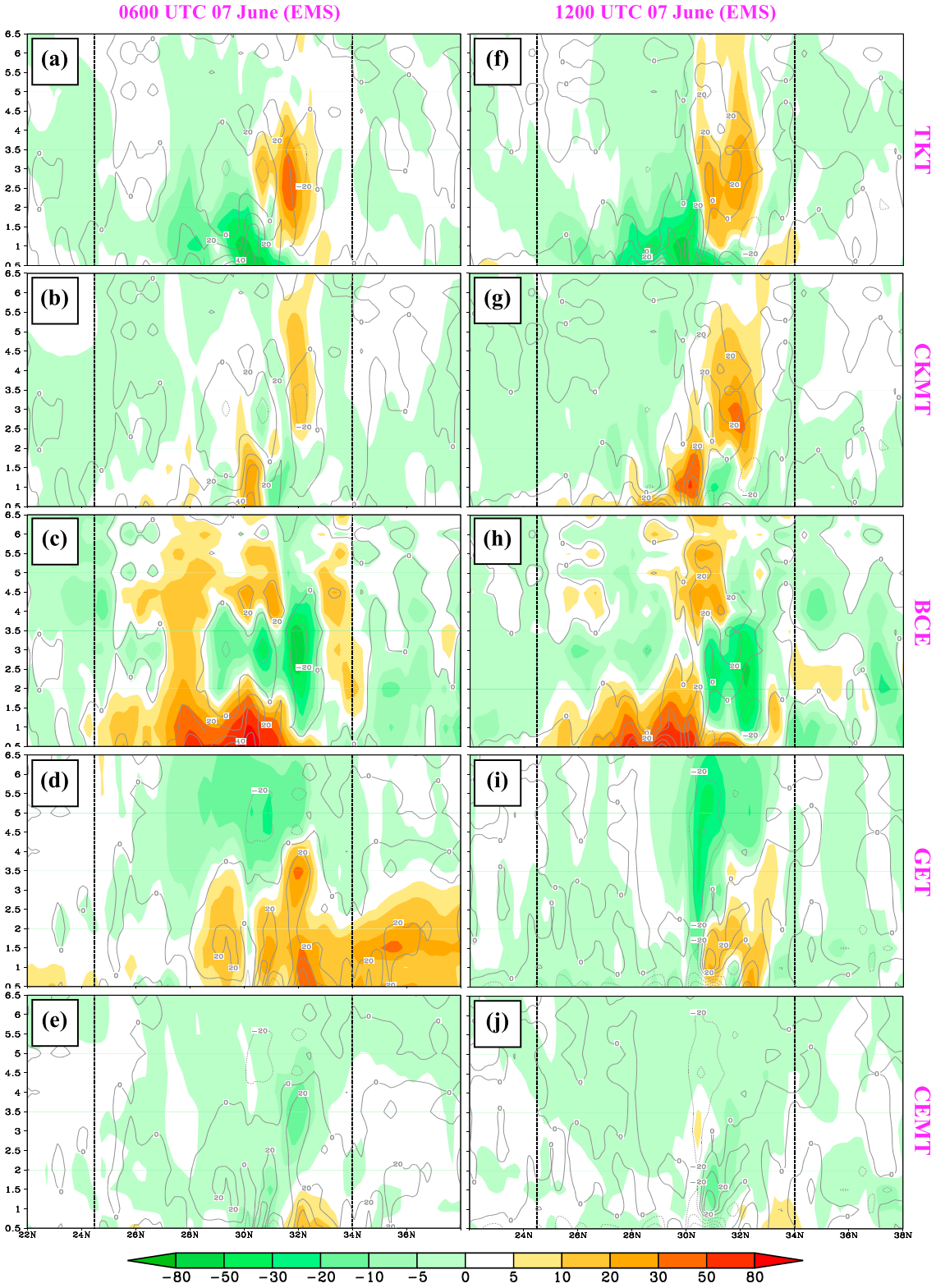


**Figure 18.** Energy budget terms (shaded) and the corresponding term TOT (grey lines) during the EMS (units: $10^{-4}$ W m$^{-3}$), where the grey solid lines mark the key area.

for the persistence of this $k_m$ center. In contrast, the strong $k_m$ regions in the south of the key area generally weakened (Figures 17c–17e). The Reynolds stress negative work on the mean flow (RSW $< 0$) was the main reason for this weakening.

The $e_m$ center to the north of the vortex persisted during the EMS (Figures 17c–17e), and the work of the mean pressure (WMP $> 0$) dominated this sustainment. In addition, the lower levels of the key area generally had a downscaled energy cascade of exergy (Table 2), which was detrimental to the persistence of $e_m$.

### 5.3. Energy Features and Budgets During the Late Maintaining Stage and Decaying Stage

#### 5.3.1. Perturbation Kinetic Energy

During the LMS and DCS, the $k_t$ associated with the vortex weakened (Figures 10f–10i and 11f–11i), corresponding to vortex attenuation. Transport by the mean and eddy flows caused net exporting of $k_t$ from the key area (TKT $< 0$), which dominated the vortex weakening during the LMS (Table 2 and Figure 19a). In contrast, the upscaled energy cascade of KE, through which energy was transferred from the vortex-related eddy flow to BCs, dominated the DCS (Table 2 and Figure 19g). Further calculation indicates that KP5 $= -\overline{\rho v'' v''} \frac{\partial}{\partial y} \langle v \rangle$ was the dominant factor for this upscaled energy cascade process (Table 2). It should be noted that term KP5 was primarily conducive to the downscaled energy cascade of KE, which favored vortex sustainment for almost the whole lifetime of the vortex, except for during the DCS (Table 2). Why then did this term change its effect during the DCS? From its expression, it is clear that the sign of KP5 is only determined by $\frac{\partial}{\partial y} \langle v \rangle$. As Figures 13a–13h show, during the DVS, EMS, and LMS, at lower levels of the key area, $\frac{\partial}{\partial y} \langle v \rangle < 0$ was associated with the vortex. This mainly corresponded to the lower-level cyclonic shear and convergent zone within the key area (Figure 9). As Figure 16 shows, at lower levels of the key area, the temperature decreased to the north. Correspondingly, the mean pressure increased to the north, which rendered a southward mean pressure gradient force. Under the influences of this southward mean pressure gradient force, the mean southerly wind at lower levels of the key area weakened gradually during the DVS and EMS; in the LMS, a mean northerly wind appeared within the northern quadrants of the vortex (Figure 13f) and enlarged with time (Figures 13f–13h); and in the DCS, the mean northerly wind zone intensified significantly and dominated the lower levels of the key area (Figure 13i). Corresponding to the above changes in the meridional wind, from the DVS to LMS, $\frac{\partial}{\partial y} \langle v \rangle$ remained negative (i.e., the BCs retained their convergent features) but decreased in intensity (as Table 2 shows, KP5 also weakened gradually). In contrast, during the DCS, $\frac{\partial}{\partial y} \langle v \rangle$ became positive (Figure 13i), which means that divergence occurred in the BCs. This significant change in the BCs caused the change from the downscaled energy cascade of KE to the upscaled energy cascade (Table 2), which triggered vortex dissipation in the DCS.

From Figure 15, it is apparent that, during the LMS and DCS, the negative vortex-related perturbation pressure center was much weaker than that of the DVS and EMS. Meanwhile, the perturbation wind field also weakened considerably during the LMS and DCS (Figure 11). Thus, the baroclinic energy conversion of the eddy flow BCE $= -\overline{\mathbf{V}_h'' \cdot \nabla_h p'}$ decreased significantly during the LMS and DCS (Table 2), but it was still favorable for the maintenance of $k_t$ at lower levels of the key area (Figures 19c and 19h and Table 2).

#### 5.3.2. Other Energies

During the LMS and DCS, $e_t$ was still at a significant level within the key area (Figures 10f–10i). At the lower levels, the work from the perturbation pressure (term WPP) and the downscaled energy cascade of exergy (Figures 19e and 19j) were the most favorable factors for the persistence of $e_t$, whereas the transport of $e_t$ by the mean and eddy flows was the most detrimental factor (not shown). At levels above 3 km, the work from the perturbation pressure (term WPP) dominated the persistence of $e_t$ (not shown), whereas the baroclinic conversion from $e_t$ to $k_t$ (Figures 19c and 19h) and the diabatic effects (Figures 19d and 19i) were the most detrimental factors to persistence.

During the LMS, the $k_m$ center to the north of the vortex still remained strong (Figures 17f–17h). This $k_m$ center mainly corresponded to the strong mean easterly wind center (Figures 13f–13h), and the baroclinic energy conversion (term BCM) was the most favorable factor for its maintenance. During the DCS, the $k_m$ center to the north of the vortex weakened rapidly (Figure 17i), mainly due to the Reynolds stress negative work (RSW $< 0$). From Figures 17f–17i, it can be observed that, during the LMS and DCS, high $k_m$ center in

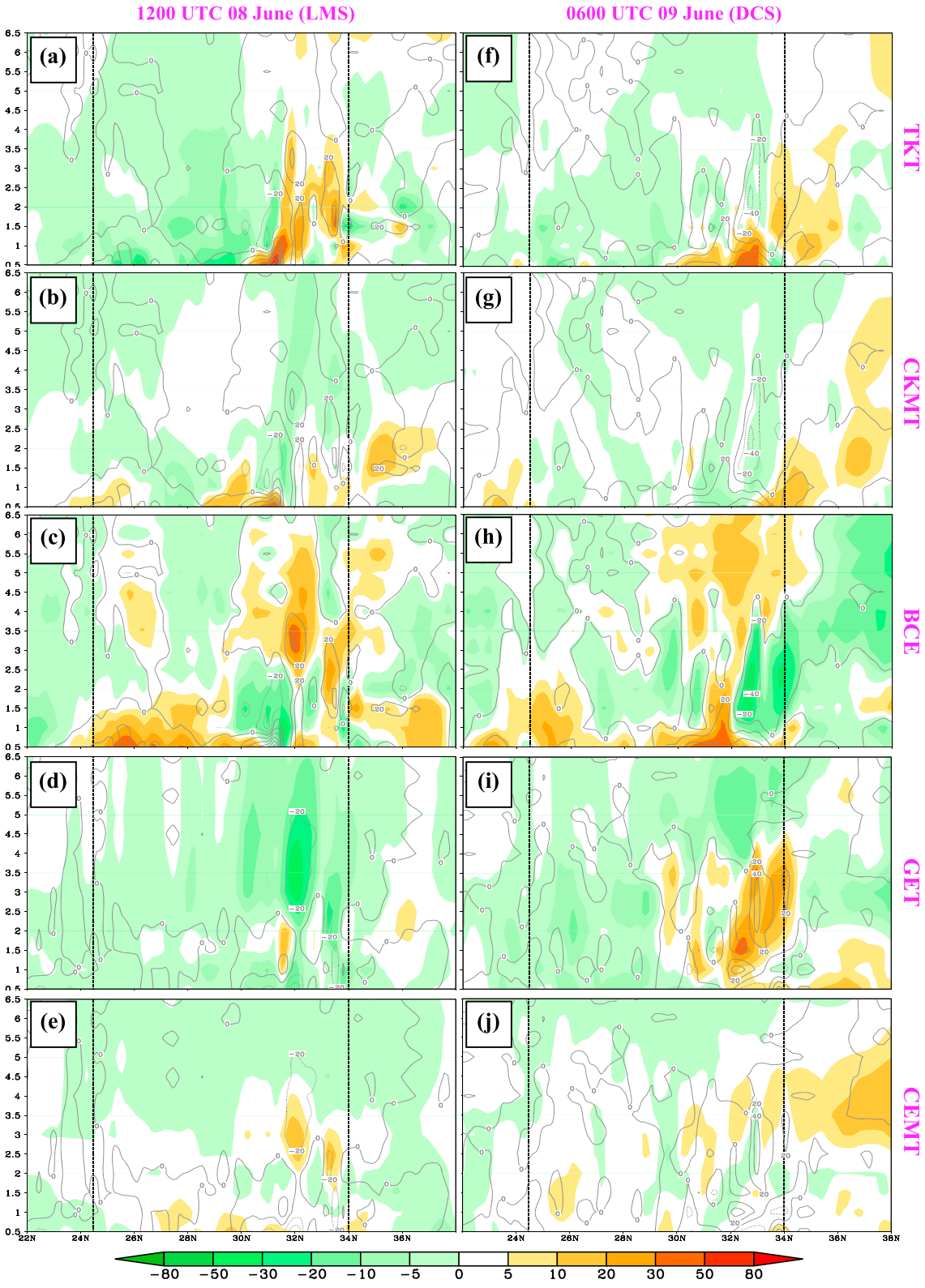


**Figure 19.** Energy budget terms (shaded) and the corresponding term TOT (grey lines) during the LMS and DCS (units: $10^{-4}$ W m$^{-3}$), where the grey solid lines mark the key area.

**Table 3.** Correlation Coefficients Between the Geometry Parameters of the Vortex and Various Vortex-Related Variables (Averaged at Heights of 1000 m and 1500 m), Where ASY, VE, ORI, $\zeta$, TOT-*cir*, PRE, and TOT-$k_t$ Represent the Asymmetry, the Vertical Extent, the Orientation, the Vorticity, the Circulation Budget TOT Term, the Observed Maximum 6-Hourly Precipitation, and the Energy Budget TOT Term, Respectively[a]

| | $\zeta$ | TOT-*cir* | $w$ | $k_t$ | $e_t$ | PRE | CKMT | CEMT | TOT-$k_t$ |
|---|---|---|---|---|---|---|---|---|---|
| $d_{max}$ | ***−0.79*** | ***−0.74*** | ***−0.62*** | ***0.45*** | 0.36 | −0.36 | −0.28 | ***0.66*** | ***−0.41*** |
| $d_{min}$ | ***−0.72*** | ***−0.63*** | ***−0.61*** | ***0.49*** | 0.24 | −0.44 | −0.11 | ***0.53*** | −0.27 |
| ASY | 0.18 | 0.05 | 0.25 | −0.28 | 0.09 | 0.08 | −0.29 | 0.09 | −0.16 |
| $r_{ef}$ | ***−0.82*** | ***−0.75*** | ***−0.64*** | 0.38 | ***0.41*** | −0.45 | −0.31 | ***0.71*** | −0.34 |
| VE | −0.28 | −0.35 | −0.13 | ***0.86*** | 0.25 | −0.05 | 0.21 | 0.13 | 0.01 |
| ORI | ***−0.79*** | ***−0.69*** | ***−0.83*** | −0.36 | 0.31 | ***−0.49*** | ***−0.61*** | ***0.41*** | ***−0.62*** |

[a]Bold italic numbers mean that the correlation exceeds the 95% confidence level.

the south of the key area (at levels above 2.5 km) weakened rapidly, corresponding to weakening of the mean southwesterly wind (Figures 13f–13i). The baroclinic energy conversion from $k_m$ to $e_m$ dominated this weakening process.

During the LMS and DCS, to the north of the vortex, $e_m$ was significant before 00:00 UTC on 09 June (Figures 17f–17h), mainly due to the work of the mean pressure (term WMP). Then, $e_m$ decreased significantly (Figures 17h and 17i), as also reflected by the variation of the isentropic surface's horizontal gradient (Figures 16h and 16i). Term ETH, which denotes the effects from the horizontal eddy transports of heat, was the dominant factor accounting for the weakening of $e_m$, because the eddy transport of heat primarily acted to weaken the temperature gradient (baroclinity) of the BCs.

## 6. Correlations Between the Vortex's Geometry and Other Key Features

The three-dimensional geometry of the vortex was closely related to the vortex's evolution. From Table 3, during the lifetime of the vortex, the vortex-averaged vorticity shows good negative correlation with the horizontal size of the vortex. This reflects the fact that the vorticity associated with the vortex would be diluted significantly by the increase in the horizontal size of the vortex. In contrast, the vertical extent of the vortex did not show a credible correlation with the lower-level vorticity. The variation rate of the vortex's circulation (which equals the surface integral of the vorticity within the vortex region) was in good negative correlation with the vortex's horizontal size. During the vortex's life span, generally, a larger horizontal size of vortex corresponded to a smaller circulation variation rate. The same was true for the $k_t$ budget TOT term. Therefore, it can be concluded that growth in the horizontal size of vortex may be favorable for vortex sustainment (due to smaller variation rate), whereas a smaller horizontal size may often mean rapid variations. This may be a possible reason why the maintaining stage, which has maximum vortex size, is much longer than the developing and decaying stages. In addition, a larger horizontal size of the vortex may also be unfavorable for the vortex mean ascending motions (convection activities) and vortex-related precipitation (Table 3). During the DVS and EMS, precipitation was heavy and mainly occurred in the quadrants to the front and right sides of the vortex's moving tracks. In contrast, during the LMS and DCS, precipitation was weak and mainly occurred in the southwestern quadrant of the vortex. For the key-area-averaged $k_t$, a greater horizontal size of the vortex meant that the vortex caused perturbations over a larger area (Figure 11); thus, there was a positive correlation between the vortex size and key-area-averaged $k_t$ (Table 3). The same was true for the key-area-averaged $e_t$. Overall, the vortex size did not show a significant correlation with the energy cascade processes of KE (vortex-BC interactions through KE), whereas for the energy cascade processes of exergy, a greater horizontal size of the vortex may favor stronger vortex-BC interactions (through baroclinic conversion of the eddy flow, these interactions can affect vortex evolution). From Table 3, it can be seen that the vertical extent of the vortex was in good positive correlation with the key-area-averaged $k_t$ (stronger perturbations could extend higher), and the vortex orientation was closely related to the vortex intensity, variation, vertical motion (convection activity), precipitation, and vortex-BC interactions. A west-east orientation of the vortex is generally favorable for the above features, except for the vortex-BC interactions through exergy. From Table 2, during the vortex's lifetime, the vortex orientation increased gradually; this may mean that the favorable conditions for the vortex sustainment reduced with time (Table 3). From Figure 5, the mesoscale vortex was elliptical but its asymmetry did not show significant

correlation with its evolution (Table 3). However, it should still be noted that during the lifetime of the vortex, the asymmetry generally had an oscillation feature under the inertially stable condition (the vortex satisfied the inertially stable condition), with a maximum and a minimum of 2.0 and 1.45, respectively.

## 7. Conclusions and Discussion

In this study, a long-lived mesoscale vortex that caused severe flash floods, landslides, and urban waterlogging in the Yangtze River Valley was successfully reproduced using the WRF model. Based on the simulations, the three-dimensional geometric features of the vortex, as well as the interactions between the vortex and its BCs, were investigated in detail.

The three-dimensional geometry of the mesoscale vortex had significant variations during the lifetime of the vortex. The effective radius of the vortex was at its minimum during the DVS (~106 km), increased in the EMS, was at a maximum during the LMS (~408 km), and decreased in the DCS. The vertical extent (represented by the bottom level pressure minus the top level pressure) of the vortex was at a minimum in the DVS (~200 hPa), was at a maximum during the EMS (~450 hPa), and then decreased gradually in the LMS and DCS. Generally, the three-dimensional geometry of the vortex was closely related to the vortex's evolution. Growth in the horizontal size of the vortex may be favorable for its sustainment, whereas a smaller horizontal size may often mean rapid variations. The vertical extent of the vortex was in good positive correlation with its perturbation KE, implying that stronger perturbations could extend higher. The vortex tended to produce stronger convection processes and precipitation as its orientation became closer to the west-east direction. In addition, during the lifetime of the vortex, the asymmetry generally had an oscillation feature under the inertially stable condition.

Circulation budgets indicate that the vortex variation displayed different mechanisms during different stages. During the DVS, the convergence-related shrinking dominated the vortex development. BC transport and the vortex moving effects accelerated development at lower and higher levels of the vortex, respectively. During the EMS, the convergence-related shrinking and BC transport dominated the vortex's persistence at lower levels, whereas the tilting effect dominated at higher levels. In addition, eddy transport mainly favored vortex sustainment. During the LMS, BC transport and divergence-related stretching rapidly weakened the vortex, whereas tilting effects and eddy transport mainly acted against attenuation. During the DCS, divergence-related stretching dominated vortex dissipation and the transport associated with the BCs and the eddy flow accelerated the attenuation. In summary, during the lifetime of the vortex, the BCs significantly affected the variation. The transport effects, the tilting effects, and the moving effects of the vortex all demonstrated the influences of the BCs.

The energy budgets of the mesoscale vortex revealed that throughout the vortex's lifetime, it interacted intensely with its BCs. The BCs affected the vortex through downscaled energy cascade processes and mean transport, and the eddy flow influenced the BCs via the upscaled energy cascade processes and eddy transport/Reynolds stress. For KE, during the DVS and EMS, the downscaled energy cascade of KE was strong, which provided energy for the development and sustainment of the vortex. The cyclonic shear and convergent BCs provided favorable conditions for the downscaled energy cascade of KE, and through the mean flow's positive work, the vortex-related eddy flow was enhanced. In addition, the baroclinic energy conversion of the eddy flow was also a dominant factor for the vortex evolution, whereas the transport effects associated with the BC and the eddy flows were the most detrimental factor that slowed down the vortex development. For exergy (which affects the vortex evolution through baroclinic conversion), the BCs' thermodynamic features, and their configuration relative to the three-dimensional eddy transport of heat, determined the vortex-BC interactions. A weak upscaled energy cascade of exergy appeared during the DVS, mainly due to the upward eddy transport of heat. In contrast, a downscaled energy cascade of exergy occurred during the EMS mainly due to the northward eddy transport of heat. However, the energy cascade process was generally weak in determining the variations of $e_m$ and $e_t$.

During the LMS and DCS, the downscaled energy cascade of KE weakened rapidly and an upscaled energy cascade appeared. This corresponded to the vortex attenuation, and the significant enhancement in the BC divergence caused the change from a downscaled to an upscaled energy cascade of KE. The transport associated with the mean and the eddy flows and the energy transfer from vortex-related eddy flow to the BCs dominated the vortex attenuation. In contrast, the baroclinic energy conversion of the eddy flow still

provided energy to vortex-related eddy flow during these two stages, which resisted the vortex decaying. For exergy, during these two stages, a downscaled energy cascade of exergy was maintained, largely due to the northward eddy transport of heat. This downscaled energy cascade was important for sustaining eddy exergy (through baroclinic energy conversion of the eddy flow, it provided energy resisting the vortex attenuation), whereas the opposite was mainly true for the transport associated with the mean and eddy flows.

In summary, during its life span, the vortex generally featured more dynamical interactions with its BCs than thermodynamical interactions. One possible reason for this was that the BCs' thermodynamical features were generally more stable than their dynamical features (cf. Figures 13 and 16) and the vortex-related perturbations were also more intense in the dynamical field (cf. Figures 11 and 15). Through vortex-BC interactions, effects from the BCs were vital for determining vortex evolution, which was consistent with the results of the circulation budget. In contrast, the variation of the BCs was mainly dominated by their own effects (e.g., the baroclinic conversion and mean transport). It should be noted that, for the evolution of BC dynamical fields, the upscaled energy cascade process of KE and the Reynolds stress effect were also important (i.e., reaction from the eddy flow cannot be ignored), whereas for the variation of BC thermodynamical fields, the eddy flow's effect was generally negligible.

**Acknowledgments**

Three anonymous reviewers provided careful comments on the submitted manuscript, which helped improve this article. The authors are grateful to the U.S. National Centers for Environmental Prediction (http://rda.ucar.edu/datasets) and the China Meteorological Administration (http://cdc.cma.gov.cn) for providing the data. Sincere thanks are extended to Fuqing Zhang for the insightful suggestions about the model configuration and for the analysis of the results. This research was supported by the National Key Basic Research and Development Project of China (2012CB417201 and 2015CB453200) and the National Natural Science Foundation of China (41205027, 41375053, and 41520104008).

## References

Akima, H. (1970), A new method of interpolation and smooth curve fitting based on local procedures, *J. ACM*, *17*, 589–602.

Black, E. (2009), The impact of climate change on daily precipitation statistics in Jordan and Israel, *Atmos. Sci. Lett.*, *10*, 192–200.

Chen, Q.-Z., Y.-W. Huang, Q.-W. Wang, and Z.-M. Tan (2007), The statistical study of the southwest vortices during 1990–2004, *J. Nanjing Univ.*, *43*, 633–642.

Davis, C. A., and T. J. Galarneau (2009), The vertical structure of mesoscale convective vortices, *J. Atmos. Sci.*, *66*, 686–704.

Ding, Y.-H., J.-J. Liu, Y. Sun, Y.-J. Liu, J.-H. He, and Y.-F. Song (2007), A study of the synoptic-climatology of the Meiyu system in East Asia, *Chinese J. Atmos. Sci.*, *31*, 1082–1101.

Fu, S.-M., and J.-H. Sun (2012), Circulation and eddy kinetic energy budget analyses on the evolution of a northeast China cold vortex (NCCV) in May 2010, *J. Meteorol. Soc. Jpn.*, *90*, 553–573.

Fu, S.-M., J.-H. Sun, S.-X. Zhao, and W.-L. Li (2011), The energy budget of a southwest vortex with heavy rainfall over south China, *Adv. Atmos. Sci.*, *3*, 709–724.

Fu, S.-M., F. Yu, D.-H. Wang, and R.-D. Xia (2013), A comparison of two kinds of eastward-moving mesoscale vortices during the Mei-yu period of 2010, *Sci. China Earth Sci.*, *56*, 282–300.

Fu, S.-M., W.-L. Li, J.-H. Sun, J.-P. Zhang, and Y.-C. Zhang (2014), Universal evolution mechanisms and energy conversion characteristics of long-lived mesoscale vortices over the Sichuan Basin, *Atmos. Sci. Lett.*, *16*, 127–134, doi:10.1002/asl2.533.

Hong, S.-Y., J. Dudhia, and S.-H. Chen (2004), A revised approach to ice microphysical processes for the bulk parameterization of clouds and precipitation, *Mon. Weather Rev.*, *132*, 103–120.

Hong, S.-Y., Y. Noh, and J. Dudhia (2006), A new vertical diffusion package with an explicit treatment of entrainment processes, *Mon. Weather Rev.*, *134*, 2318–2341.

Hu, B.-W., and E.-F. Pan (1996), Two kinds of cyclonic disturbances and their accompanied heavy rain in the Yangtze River Valley during the Meiyu period, *J. Appl. Meteorol. Sci.*, *7*, 138–144.

James, E. P., and R. H. Johnson (2010), Patterns of precipitation and mesolow evolution in midlatitude mesoscale convective vortices, *Mon. Weather Rev.*, *138*, 909–931.

Kain, J. S., and J. M. Fritsch (1990), A one-dimensional entraining/detraining plume model and its application in convective parameterization, *J. Atmos. Sci.*, *47*, 2784–2802.

Karl, T. R., and R. W. Knight (1998), Secular trends of precipitation amount, frequency, and intensity in the United States, *Bull. Am. Meteorol. Soc.*, *79*, 231–241.

Kirk, J. R. (2003), Comparing the dynamical development of two mesoscale convective vortices, *Mon. Weather Rev.*, *131*, 862–890.

Kucharski, F., and A. J. Thorpe (2000), Local energetics of an idealized baroclinic wave using extended exergy, *J. Atmos. Sci.*, *57*, 3272–3284.

Kuo, Y.-H., L.-S. Cheng, and J.-W. Bao (1988), Numerical simulation of the l981 Sichuan flood. Part I: Evolution of a mesoscale southwest vortex, *Mon. Weather Rev.*, *116*, 2481–2504.

Lu, J.-H. (1986), *Generality of the Southwest Vortex*, 270 pp., China Meteorol. Press, Beijing.

Michalakes, J., J. Dudhia, D. Gill, T. Henderson, J. Klemp, W. Skamarock, and W. Wang (2004), The Weather Research and Forecast model: Software architecture and performance, to appear in Proceedings of the Eleventh ECMWF Workshop on the Use of High Performance Computing in Meteorology, 25–29 October.

Ninomiya, K. (2000), Large-and meso-α-scale characteristics of Meiyu/Baiu front associated with intense rainfalls in 1–10 July 1991, *J. Meteorol. Soc. Jpn.*, *78*, 141–157.

Orlanski, I. (1975), A rational subdivision of scales for atmospheric processes, *Bull. Am. Meteorol. Soc.*, *56*, 527–530.

Qian, T.-T., P. Zhao, F.-Q. Zhang, and X.-H. Bao (2015), Rainy-season precipitation over the Sichuan Basin and adjacent regions in southwestern China, *Mon. Weather Rev.*, *143*, 383–394, doi:10.1175/MWR-D-13-00158.1.

Rudeva, I., and S. K. Gulev (2007), Climatology of cyclone size characteristics and their changes during the cyclone life cycle, *Mon. Weather Rev.*, *135*, 2568–2587.

Saha, S., et al. (2010), The NCEP Climate Forecast System Reanalysis, *Bull. Am. Meteorol. Soc.*, *91*, 1015–1057.

Shen, X.-Y., Y.-Q. Ni, M. Zhang, N. Zhao, and L.-X. Peng (2005), A possible mechanism of the genesis and development of meso-β rain storm system. Part I. Phase velocity of vortex Rossby waves, *Chin. J. Atmos. Sci.*, *29*, 727–733.

Speer, M. S. (2008), On the late twentieth century decrease in Australian east coast rainfall extremes, *Atmos. Sci. Lett.*, *9*, 160–170.

Stevenson, S. N., and R. S. Schumacher (2014), A 10-year survey of extreme rainfall events in the central and eastern United States using gridded multisensor precipitation analyses, *Mon. Weather Rev.*, *142*, 3147–3162.

Sun, J.-H., S.-X. Zhao, G.-K. Xu, and Q.-T. Meng (2010), Study on a mesoscale convective vortex causing heavy rainfall during the Mei-yu season in 2003, *Adv. Atmos. Sci.*, *27*, 1193–1209.

Tao, S.-Y. (1980), *Rainstorms in China*, 225 pp., Sci. Press, Beijing.

Tao, S.-Y., and Y.-H. Ding (1981), Observational evidence of the influence of the Qinghai–Xizang (Tibet) Plateau on the occurrence of heavy rain and severe convective storms in China, *Bull. Am. Meteorol. Soc.*, *62*, 23–30.

Wang, Q.-W., and Z.-M. Tan (2014), Multi-scale topographic control of southwest vortex formation in Tibetan Plateau region in an idealized simulation, *J. Geophys. Res. Atmos.*, *119*, 11,543–11,561, doi:10.1002/2014JD021898.

Yang, Y.-M., W.-L. Gu, R.-L. Zhao, and J. Liu (2010), The statistical analysis of low vortex during Meiyu season in the lower reaches of the Yangtze, *J. Appl. Meteorol. Sci.*, *21*, 11–18.

Zhao, S.-X., and S.-M. Fu (2007), An analysis on the southwest vortex and its environment fields during heavy rainfall in eastern Sichuan Province and Chongqing in September 2004, *Chin. J. Atmos. Sci.*, *31*, 1059–1075.

Zhao, S.-X., Z.-Y. Tao, J.-H. Sun, and N.-F. Bei (2004), *Study on Mechanism of Formation and Development of Heavy Rainfalls on Meiyu Front in Yangtze River*, 282 pp., China Meteorol. Press, Beijing.